Gate Potential Control of Nanofluidic Devices

by

Arnaud Le Coguic

Submitted to the Department of Electrical Engineering and Computer Science
in partial fulfillment of the requirements for the degree of

Masters of Science in Electrical Engineering and Computer Science

at the

MASSACHUSETTS INSTITUTE OF TECHNOLOGY

June 2005

© Massachusetts Institute of Technology 2005. All rights reserved.

Author .....
Department of Electrical Engineering and Computer Science
May 6, 2005

Certified by .....
Jongyoon Han
Assistant Professor
Thesis Supervisor

Accepted by .....
Arthur C. Smith
Chairman, Department Committee on Graduate Students

BARKER

MASSACHUSETTS INSTITUTE OF TECHNOLOGY
OCT 2 1 2005
LIBRARIES

Gate Potential Control of Nanofluidic Devices

by

Arnaud Le Coguic

Submitted to the Department of Electrical Engineering and Computer Science
on May 6, 2005, in partial fulfillment of the
requirements for the degree of
Masters of Science in Electrical Engineering and Computer Science

Abstract

The effect of an external gate potential control on the nanofluidic nanochannels was experimentally investigated in this work. Like in the field effect transistors (FET) in microelectronics, molecular transport in micro/nanofluidic channels can be controlled by applying external potentials on the wall of the fluidic channel. In nanofluidic devices, this type of control is expected to be more efficient due to its high surface to charge ratio. We focused on a nanofluidic concentrator to study this effect. We could increase or decrease the concentration rate of the device by increasing or decreasing the surface charge potential (ζ-potential) on the walls of the nanochannels. An increased ζ-potential enhances the electrokinetic effects caused by electrical double layer. Which in turn accelerates the creation of a charge polarization region and improves the concentration capabilities of the device. We also have demonstrated concentration polarization effect, caused by pressure-driven flow in the nanofluidic channel, and showed that this phenomena can also be modulated by changing the gate potential of the nanofluidic devices. The gate potential effect opens the door for closed-loop real-time control of nanofluidic concentrators.

Thesis Supervisor: Jongyoon Han
Title: Assistant Professor

Acknowledgments

I would like to thank Professor Han for trusting me, giving me the privilege of collaborating with him and for allowing me to benefit from his drive and cleverness. I am thankful for the numerous lessons he taught me. Sincere thanks also go to the funding sources that made it possible for me to do this research work: the MIT Rosenblith Presidential Fellowship, the National Science Foundation CTS division through its grants CTS-0347348 and CTS-0304106.

I would also like to thank all the professors that influenced me along the way, at Lycée Louis-le-Grand, Ecole Polytechnique and MIT; their sharpness of mind inspired me to make all the possible efforts to achieve both precision and clarity, depth and perspective.

I would also like to thank all the labmembers-turned-friends who greatly contributed to the learning experience that this thesis proved to be. Yong-Ak Song, Jianping Fu, Hansen Bow, Pan Mao, Wendy Gu, Aleem Siddiqui, Salil Desai and all the others. I thank you for being the nice and interesting people that you are. Let me also thank Ying-Chih Wang for fabricating the silicon devices used in this thesis.

I would like to thank my close family for instilling in me values that still guide me today.

Finally, some goals are better set and achieved when seen through the eyes of shared enthusiasm, happiness and aspirations. And I thank you, Hanh, for bringing me all this.

Contents

List of Figures

List of Tables

Chapter 1

Introduction

Nanobiotechnology holds considerable promise of advances in the pharmaceutical and health care industries as well as for chemical assays, environmental analyses, materials assessments and measurements in harsh environments. This versatility of nanobiotechnology is partly attributable to its positioning at the junction of physical sciences, materials sciences, biology and chemistry.

Reducing the scale by several orders of magnitude to go from macrodevices to devices of the order of the nanometer enables us to work on the scale that is relevant to molecular phenomena. Nanodevices have already been developed to manipulate, sort, identify and quantify the presence of important biomolecules like proteins, RNA, DNA, hormones, ions ([1–6]).

In the micro- and nanosystems for chemical and biological analysis, scale reduction brings substantial benefits ([7–9]). The amount of reagents and samples needed are greatly reduced. The reduced timescale aids in controlling chemical reactions by providing more accurate and faster fluid handling. Temperature is easier to control for small quantities of matter. Automated total analysis systems, that can deliver, mix, concentrate and separate fluids, eliminate labor-intensive bench top processes and the possible errors associated with them. Finally, the technology provides great promise in improving sensitivity, specificity and the processing time required, which are the key requirements for modern biomedical sample analysis.

Microfluidics have been intensively studied for the past decade ([7]). Now some

groups are studying nanometer scale devices ([10–12]). But some properties of nanofluidics remain ill-known today and could allow the development of new techniques to perform novel functions. One such phenomenon is the charge dependent transport of molecules when driven through a nanochannel hindered by overlapping double layers ([13–15]). In nanometer-size channels, effects of Debye layers are not negligible, unlike in microfluidic channels. These unique properties of nanochannels can be used to provide original tools for molecular analysis. Moreover, in nanochannels, fluidic and molecular transport properties will be heavily affected by the surface potential. While the modulation of microfluidic device by external voltage control of surface potential has been done previously ([16]), this 'gate potential' control is anticipated to be more effective in nanochannels because of their larger surface-to-volume ratios.This mode of control would be more effective in nanofluidic than microfluidic devices, due to significant overlap of double layers. Moreover, when thinking of a nanofluidic concentrator, an external control of double layer thickness would bring a real time adaptability of concentration rate that has not been demonstrated with other preconcentration schemes (differential mobilities method, adsorption on stationary or pseudo-stationary phases method)

In this thesis, we will test this gate-potential control of nanochannels using the nanofluidic preconcentrator as a model system. We will first review the background knowledge relevant to the mechanism at stake and review the literature previously published on adjacent topics (Chapter 2). External voltage control has already been studied for the modification of electroosmotic flow, mainly in capillaries and microfluidic devices ([16–18]). As opposed to coating ([19]) or buffer alterations ([20]), this external voltage control allows for real-time control on the double layer, which determines many important electrokinetic properties of nanofluidic devices. We will then present a preliminary experiment in a deep nanochannel PDMS device. From that point on, we will work on a nanofluidic concentrator ([21]) as a model nanofluidic device. Initially characterizing its behavior as the gate voltage is floated (Chapter 4). Then the operation efficiency of the nanofluidic concentrator with different gate potential applied to the substrate was studied (Chapter 5). We also characterized

another mode of operations for the nanofluidic concentrator: one that uses a pressure driven flow (Chapter 6). And finally we investigated the response of concentration rates in case of a pressure-driven flow to varied gate voltages (Chapter 7).

Chapter 2

Background

Fluid and molecules in fluids exhibit unique properties that are not readily visible or appreciated in the larger scale fluidic channel. Understanding transport phenomena, double layers behavior, the solutions properties as well as some properties of dielectric materials like SiO_2 is key to developing better nanofluidic tools and devices. In this chapter, we will review the basic theoretical concepts necessary to understand the nanofluidic phenomena related to the preconcentrator's external control, as well as previous experimental and theoretical research in the area of nanofluidics.

2.1 Theory on electrokinetics and double layers

2.1.1 Electrical double layer

If a solution of ions is in contact with a charged surface, the ions close to that surface migrate, and electro-neutrality is locally violated. The zone where the net local charge density is not zero is called the electrical double layer, or double layer in short. In the double layer, the amount of electric charge equals the charge on the wall. The counter-ions adsorbed on the wall compose the Stern layer, and the counter-ions present further from the wall form the diffuse layer. The two layers together constitute the double layer. In a typical physiological solution, its thickness is in the order of 1nm. The ζ-potential is the potential at the slip boundary (figure

2-1), which is the interface between the Stern and diffuse layers ([22]).

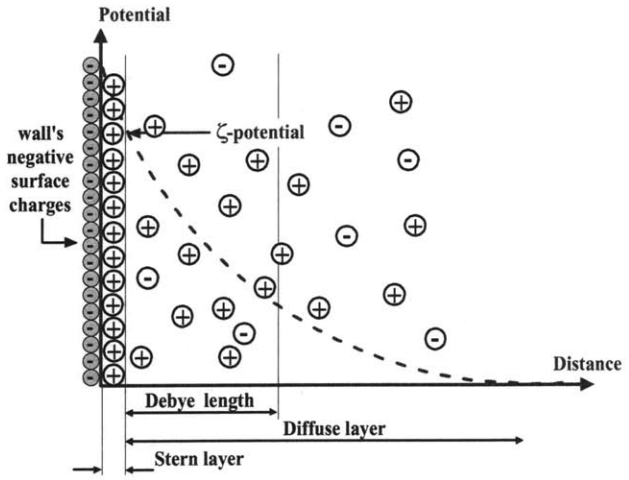

Figure 2-1: Helmholtz double layer. White disks represent free ions in solution.

The double layer thickness is defined as κ^{-1} with:

$$\frac{1}{\kappa} = \sqrt{\frac{\epsilon_0 \epsilon_r RT}{F^2 \sum_i c_i z_i^2}}$$

with ϵ_0 and ϵ_r: respectively the permittivity of vacuum and the static relative permittivity of the solution; R: gas constant; T: thermodynamic temperature, F: Faraday constant; c_i: concentration of species i; z_i: ionic charge of species i. .

If we make a rough evaluation of the Double layer thickness for a monovalent electrolyte with a concentration of 1mM:

$$\begin{aligned} \frac{1}{\kappa} &= \sqrt{\frac{\epsilon_0 \epsilon_r RT}{F^2 \sum_i c_i z_i^2}} \\ &= \sqrt{\frac{8.85 \times 10^{-12} \cdot 80 \cdot 8.314 \cdot 300}{96500^2 \cdot 10^{-3} \cdot 1000 \cdot 1^2}} \\ &\simeq 14nm \end{aligned}$$

This calculation shows us that in a nanochannel of the order of 30nm deep, the

Molarity (mole.L^{-1})	z_+:z_-	Symmetrical electrolyte (m)	z_+:z_-	Asymmetrical electrolyte (m)
0.001	1:1	9.61×10^{-9}	1:2, 2:1	5.56×10^{-9}
0.001	2:2	4.81×10^{-9}	1:3, 3:1	3.93×10^{-9}
0.001	3:3	3.20×10^{-9}	2:3, 3:2	2.49×10^{-9}
0.01	1:1	3.04×10^{-9}	1:2, 2:1	1.76×10^{-9}
0.01	2:2	1.52×10^{-9}	1:3, 3:1	1.24×10^{-9}
0.01	3:3	1.01×10^{-9}	2:3, 3:2	7.87×10^{-10}
0.1	1:1	9.61×10^{-9}	1:2, 2:1	5.56×10^{-10}
0.1	2:2	4.81×10^{-10}	1:3, 3:1	3.93×10^{-10}
0.1	3:3	3.20×10^{-10}	2:3, 3:2	2.49×10^{-10}

Table 2.1: Double layer thicknesses, κ^{-1}, for several electrolyte concentrations and valences.

presence of the double layers would not be negligible.

Modification of the electrokinetic effects caused by the Debye layer

The double layer exists to offset the surface charge on the wall in contact with the solution. As the surface charge density is increased, the ζ-potential will increase. A higher ζ-potential results in a higher intensity of electrokinetic effects caused by the Debye layer. Reversely, if the surface charge density is decreased, the ζ-potential is decreased and the electrokinetic effect caused by the Debye layer are reduced. In the limit case where the surface charge density on the wall is zero, no counterions are needed to shield any charge and no double layer exists. Thus if we can control the **surface potential**, we will be able to control the effects of the Debye layer.

Concurrently, for a given surface potential of the channel's walls, the more concentrated the ions in solution, the thinner the double layer necessary to shield the surface wall charge. The ionic strength of a measure of the buffer solution's ability to screen electrostatic charges. For a solution containing N species with molar concentrations c_i and charges z_i, it is defined as

$$\frac{1}{2}\sum_{i=1}^{N} c_i z_i^2.$$

Then one can state that the double layer thickness κ^{-1} decreases when the **ionic strength** of the solution is increased.

2.1.2 Electroosmosis

Electroosmosis is the movement of an electrolyte solution relative to a stationary charged surface due to an applied electric field. The applied electric field tangential to the double layer surface applies a force on the mobile double layer of counter-ions. The counter-ions drag the electrolyte solution and flow occurs towards the electrode whose charge is opposite to that of the counter-ions. The electroosmotic flow is related to the ζ-potential by the Helmholtz-Schmoluchowski equation:

$$\overrightarrow{v}_{EOF} = -\zeta \frac{\epsilon_b}{\eta_0} \overrightarrow{E}_{app}$$

where ϵ_b is the permittivity of the buffer, η_0 is the viscosity of the buffer and E_{app} is the applied electric field ([13]).

2.1.3 Electrophoresis

Electrophoresis is the motion of a charged particle in solution, due to an applied electric field. Electrophoresis drives a negatively charged molecule towards the anode and a positively charged molecule towards the cathode. We can prove rigorously the relation between the electrophoretic velocity $\overrightarrow{v}$ and the applied field $\overrightarrow{E}_{app}$ to be ([23]):

$$\overrightarrow{v} = [\frac{\frac{\epsilon\zeta}{\eta}}{1 + \frac{\epsilon\zeta\sigma_m}{\eta\sigma R}}] \overrightarrow{E}_{app}$$

where σ_m represents all the mobile charges in the double layer, ϵ is the permittivity of the solution, ζ represents the zeta-potential, η is the viscosity of the solution.
This motion is due to 'the coupling in the mobile part of the double layer, where viscous and electrical shear stresses balance in a manner similar to that of electroosmotic flow, resulting in a relative motion between fluid and particle' ([23]).

2.1.4 Electrical resistance and capacitance of the channel filled with buffer

We know the expression for the **electrical resistance** of a channel filled with solution:

$$R = \frac{\rho_{solution} \times l}{S}$$

where ρ is the resistivity of the solution, l the length of the channel and S the area of its cross-section. We can then evaluate the resistance of the 50 PDMS nanochannels (3-1)in parallel filled with 0.1M KCl buffer. The conductivity of this buffer can be found in the literature ([24]):

$$\begin{aligned} R_{nanoPDMS} &= \frac{1}{50} \cdot \frac{66 \cdot 1 \times 10^{-5}}{1.5 \times 10^{-7} \cdot 1 \times 10^{-5}} \\ R_{nanoPDMS} &= 8.8 \times 10^{6} \Omega \end{aligned}$$

We can also evaluate the electrical resistance of the channel between reservoir 1 and 2 in the silicon device (figure 2-3), filled with phosphate buffer at 1mM. The conductivity of this buffer is also found in the literature ([24]).

$$\begin{aligned} R_{chSi} &= \frac{5.88 \cdot 8.5 \times 10^{-3}}{1.5 \times 10^{-6} \cdot 10 \times 10^{-6}} \\ R_{chSi} &= 3.3 \times 10^{9} \Omega \end{aligned}$$

The **capacitance** of two parallel identical plates of surface A and separated by a medium with dielectric permittivity $\epsilon = \epsilon_0 \epsilon_r$ with thickness d:

$$C = \frac{A \epsilon_0 \epsilon_r}{d}$$

where ϵ_r is the relative permittivity of the medium and $\epsilon_0 = 8.85 \times 10^{-14} F/cm$ is the dielectric permittivity of vacuum.

We can then calculate the capacitance corresponding to a 250nm thick SiO_2 layer

between gold electrodes and a PDMS channel:

$$\begin{aligned} C &= \frac{A\epsilon_0\epsilon_r}{d} \\ C &\approx \frac{0.5cm \cdot 3cm \cdot 8.85 \times 10^{-14} \cdot \epsilon_r}{250nm} \\ C &\approx 4.5nF \end{aligned}$$

Similarly, if we liken the channels of the silicon device described below (in the 'silicon device experiment' chapter) to two infinite parallel plate, we can calculate the capacitance of the device:

$$\begin{aligned} C &= \frac{A\epsilon_0\epsilon_r}{d} \\ C &\approx \frac{15\mu m \cdot 8cm \cdot 8.85 \times 10^{-14} \cdot \epsilon_r}{500nm} \\ C &\approx 17pF \end{aligned}$$

2.1.5 EOF flow vs. pressure driven flow

Electroosmotic flow profile calculation The flow of a viscous newtonian fluid is described by the Navier-Stokes equation. This equation states that if we consider a parcel of fluid, its mass times acceleration has to equal, according to Newton's laws of motion, the sum of the forces it undergoes: the viscous forces, the pressure gradient force and the electrical force.

$$\mu \frac{D\vec{v}}{Dt} dV = (\eta \nabla^2 \vec{v} - \nabla p + \rho \vec{E}) dV$$

with μ the fluid's density , η its dynamic viscosity and ρ is the charge density. Let us moreover consider the pressure gradient to be zero, and introduce the Reynolds number, defined as $Re = \frac{\mu v_s L}{\eta}$ with v_s the mean fluid velocity, L the characteristic length of the system. We know that the Reynolds numbers in micro and nanofluidic systems are orders of magnitude less than one. And the Reynolds number is also the ratio of the inertial term of the Navier-Stokes equation to the viscous term. So in the

case a micro or nanofluidic system, we can neglect the inertial term and since

$$\rho\vec{E}dV = -\rho\nabla\psi dV$$

we can finally write the Navier-Stokes equation:

$$\vec{0} = (\eta\nabla^2\vec{v} - \rho\nabla\psi)dV$$

In a long cylinder along axis x with radius a, the equation can be expanded thus

$$\frac{\mu}{r}\frac{\partial}{\partial r}(r\frac{\partial v_x}{\partial r}) = -\frac{\epsilon}{r}\frac{\partial}{\partial r}(r\frac{\partial\psi}{\partial r})E_x$$

where r is the distance to the center of the cylinder and x the distance from one reference end of the cylinder, E_x is the driving electric field along the channel and ψ the local electric potential. This equation can be integrated under the following electrokinetic boundary conditions

$$\begin{aligned} \frac{\partial v_x}{\partial r} = 0 \text{ and } \frac{\partial\psi}{\partial r} = 0 \qquad & \text{at } r = 0 \\ v = 0 \text{ and } \psi = \zeta \qquad & \text{at } r = a \end{aligned}$$

and the result is

$$v_x(r) = -\frac{\epsilon(\psi - \zeta)}{\mu}E_x$$

In the case of a thin Debye layer, $\psi = 0$ for most of the cross-section and we just need to solve ψ near the capillary wall. Call λ_D the Debye layer thickness. Close to the wall, we can neglect the curvature effect ($a \gg \lambda_D$) and we are left with solving the one-dimensional problem:

$$\frac{\partial^2\psi^*}{\partial y^{*2}} = sinh\psi^*$$

where $y^* = y/\lambda_D$. A Debye-Hückel linearization gives the following solution

$$\psi = \zeta e^{-(a-r)/\lambda_D}$$

so we finally obtain the expression of the flow profile:

$$v_x(r) = -\frac{\epsilon\zeta}{\mu}(1 - e^{-(a-r)/\lambda_D})E_x$$

This equation that for r such that $a - r \gg \lambda_D$, the flow profile is almost flat.

Pressure flow profile calculation The parameters determining a pressure flow profile are the viscosity of the fluid, the difference between pressures applied at the 2 ends of the channel and the dimensions of the channel. Let's consider a cylindrical channel. Newton's second law of motion can be written:

$$\frac{d}{dr}[2\pi r L\mu(\frac{dv_x}{dr})]dr = -2\pi r\Delta p dr.$$

Integrating once, we find

$$2\pi r L\mu\frac{dv_x}{dr} = -2\pi(r^2/2)\Delta p \text{ or } \frac{dv_x}{dr} = -(\frac{\Delta p}{2L\mu})r + A,$$

where A is a constant. By symmetry, when r = 0, dv/dr = 0, so A = 0. Integrating a second time,

$$v_x(r) = -\frac{\Delta p}{4L\mu}r^2 + B = 0,$$

where B is a second constant of integration. Since v = 0 when r = a, the evaluation of B gives

$$v_x(r) = \frac{\Delta p}{4L\mu}(a^2 - r^2),$$

which is the parabolic velocity profile of Poiseuille flow.

Electroosmotic vs. pressure flow profiles The EOF flow profile is flat as opposed to the flow created by pressure on (viscous) fluids that is parabolic with a the fluid in contact to the walls motionless relative to these walls.

2.2 Relevant prior research on nanofluidics

2.2.1 Experimental observation of externally applied potential on EOF

Externally applied potentials as a way to control electrokinetic phenomena have been used in the past, mainly in capillary systems and microfluidics. Its effect on the electroosmotic flow as been thoroughly investigated:

- in various substrates such as glass capillaries ([17, 18, 25, 26]), PDMS([27]) and silicon devices ([16])
- for ever larger pH ranges, in which this control is still feasible. It was found that external voltage control was easier at lower pH (pH=1.4) than for higher pH (pH=6.3). Furthermore the relationship between the applied voltage and the electroosmotic flow appears to be sigmoidal over a wide range of flow velocities for low pH's and linear over a narrower range of flow velocities for high pH's. (from[1,3] to [1,7]) ([20, 28])
- with ever smaller external potential applied. A microfabricated device with electrodes $50\mu m$ from the inner walls of the channel, demonstrated an electroosmotic flow control 50 to 80 times more efficient than in usual capillaries. 120V were sufficient to induce significant changes in flow velocity, as opposed to several thousands of volts before ([18])

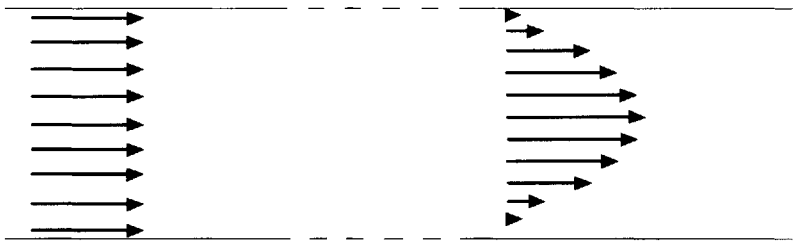

Figure 2-2: Comparison of the flow profiles for an electroosmotic flow (left) and a pressure-induced flow (right).

- in more diversified buffer solutions: potassium phosphate, potassium chloride, potassium bromide, potassium fluoride, potassium iodate, potassium nitrate, potassium nitrite, potassium sulfate, potassium acetate, maleic acid, malonoic acid, tartaric acid, citric acid, oxalic acid ([29])

- for various surface properties and surface modifications by coating ([19] [20]). When cationic surfactants are added to the buffer, they effectively make the wall charge positive and reverse the electroosmotic flow.

All these work contribute to forming a good understanding of the external voltage control.

2.2.2 Theoretical models for externally applied voltages

Three main theories were developed to explain external voltage control:

- an electrostatic-based model ([28, 30]). When applied to a fused silica capillary with inner diameter R_i and outer diameter R_o, permittivity ϵ_Q and if the externally applied voltage V_{ext} creates a surface charge $\sigma_{V_{ext}}$ on the inner wall of the capillary, then we can express $\sigma_{V_{ext}}$ as a function of V_{ext}: $\sigma_{V_{ext}} = (\epsilon_Q V_{ext/R_i})(-ln(R_i/r_o))$ and then the velocity of the electroosmotic flow as a function of $\sigma_{V_{ext}}$:

$$v_{EOF} = \frac{\epsilon_b}{\eta_0} E_{app} exp(-\kappa x) \frac{2kT}{e} \times \sin^{-1}((\sigma_{V_{ext}} + \sigma_{Si}) \sqrt{\frac{500\pi}{\epsilon_b RCT}})$$

- a Gaussian-based model: arbitrary magnitudes are used for variables to adjust the outcome to match the experimental data. For example the diffuse double layer is arbitrarily fixed while the ionic strength is set to adjust the model to the initial flow rate ([29, 30]). The electroosmotic mobility is written $\mu_{eo} = \mu_{eo}^0 + \mu_{eo}^{V_{ext}}$, with $\mu_{eo}^{V_{ext}} = -\frac{\epsilon_0 \epsilon_{aq}}{\eta} \Phi(\delta)$ with $\Phi(x)$ can be evaluated as a function of the surface charge density in the diffuse layer σ_d:

$$\phi(x) = \frac{2kT}{ze} ln(\frac{[1 + S + (1 + S^2)^{1/2}][1 + exp(-\kappa x)] - 2exp(-\kappa x)}{[1 + S + (1 + S^2)^{1/2}][1 - exp(-\kappa x)] + 2exp(-\kappa x)})$$

with S defined for convenience as $S = \frac{\sigma_d}{(8kT\epsilon_{aq}\epsilon_0 n^0)^{1/2}}$

- a Multi-Ion Model ([31]). This method solves simultaneously for the concentration field, a single potential field, the flow field and the pressure field. We use the dilute solution model (DSM) to get the flux of ions, the Poisson-Boltzman equation for the potential, the Navier-Stokes (including a Lorentz term force) for the velocity and pressure in the solvent.

  The solution is calculated using a finite element method.

Numerical simulations of externally altered EOF have been performed based on these models ([32,33]).

The predictive capabilities of the electrostatic and Gaussian based models were compared to the experimental results of external voltage control in the literature by Hartley and Hayes ([30]). If both models bring theoretical explanations and can help predict trends, their accuracies for various implementations (ionized air, conductive sheath, concentric capillaries, parallel plates) and geometries (percentage of coverage of the external electrode) are very limited.

It is important to realize that calculation and simulation of EOF by the superposition of two potential distributions is widely used ([34]). It is also part of the electrostatic and Gaussian-based models. However this approach is not valid in geometries for which the characteristic dimensions are comparable to the Debye length.In this specific case the multi-ion model has to be used.

2.2.3 Debye layer thickness greater than the channel's thickness

Numerical simulations by Daiguji et al. ([35]) suggest that when the diameter of a capillary is smaller than the Debye length, only counterions are present in this portion of the capillary. Electrostatic interactions prevent coions from entering the thick Debye layer zone ([35,36]). 3 parameters were varied: the potential difference between the 2 ends of the channel, the surface charge density and the bulk ion concentration.

As the potential bias is increased, the electric field strength inside the channel increases, but not linearly. Concurrently the concentration of ions inside the nanochannel increases. More over, if one calculates the ionic currents, they notice that the counter-ion current is increased with the potential bias, whereas the co-ion current remains almost un-altered.

If the surface charge is set to zero in their simulation, the differences in co- and counter-ion concentrations inside the channel, as well as the differences in ionic currents vanish. Whereas an increase in surface charge is calculated to increase the difference in co- and counter-ions concentrations inside the channel and current through the channel.

Finally, it was calculated that the lower the bulk solution concentration, the larger the difference in ion concentration and in ionic currents through the channel.

These theoretical calculations based on the Poisson-Nernst-Planck equations have not been tested by the authors in an actual device.

2.2.4 Nanofluidic filter Preconcentrator

The device I will be using was conceived by a labmate in Professor Han's group, Ying-Chih Wang ([21]). Concurrently to my experiments using externally applied voltages, he investigated the concentration factors that could be reached by this device for proteins and peptides samples. Concentration factors up to 10^7 were demonstrated within 1 hour when starting with femto-molar GFP samples. Figures 2-3, 2-4 and picture 2-5 represent the geometry of the device.

2.3 Our proposal

Our proposal is to use external voltage control to improve the control and performances of a nanofluidic preconcentrator. The surface as an electrode would allow us

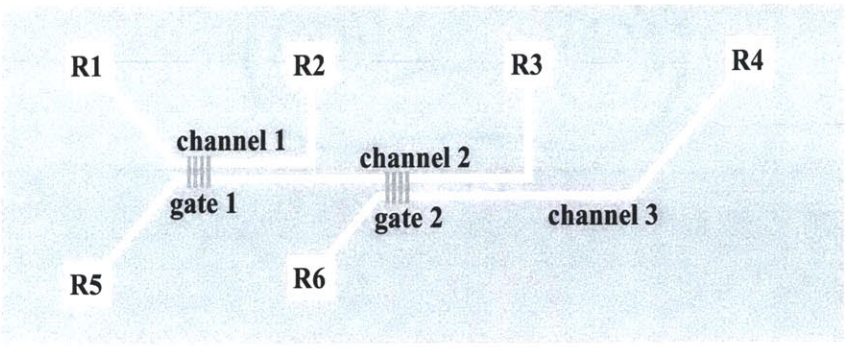

Figure 2-3: Top view of the silicon device.

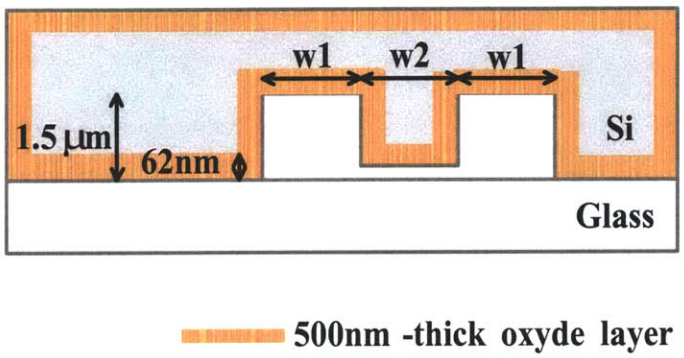

Figure 2-4: Cross-section of the silicon device.

to modify the surface charge density inside the nanofluidic channel, by applying a potential through a dielectric layer. We will then test the concentration rates and factors that we can obtain when the gate potential is changed. We will measure the effect of this gate potential for several driving mechanisms: electrokinetics as well as pressure. Additional Measurements of the width of the depletion region and of the influence of the buffer ionic strength will confirm the hypothesis that we are controlling the zeta potential in the double layer to control the (nonlinear) electrokinetic behavior.

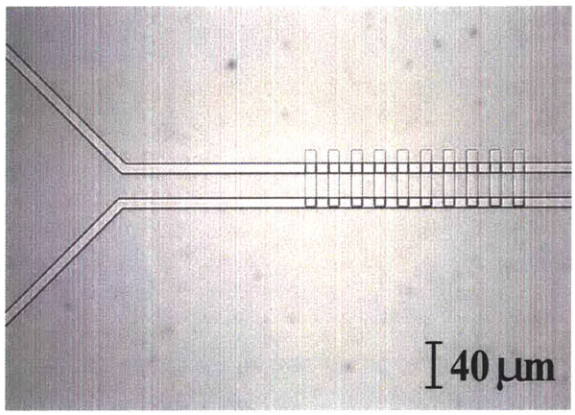

Figure 2-5: Bottom view of the silicon device conceived by Ying-Chih Wang, centered on the nanofilters region.

Chapter 3

Study of gate-potential control of nanofluidic channels in PDMS nanochannels

We started our investigation of the possible filtering effect of Debye layers hindering part of a shallow filter region, by making and using PDMS nanochannels. They presented the advantage of being easy and cheap to produce in large numbers. Their drawback is the speed at which they deteriorate and the difficulty to make very shallow channels that don't collapse (less than 150nm) ([37]).

3.1 Design and working principle

We want to create an electroosmotic flow of charged particle in the deep channels. In the middle of the way though, we place a 'filter' through which all particle have to go. Additionally, an electrode is placed below the shallow region, so that we can control its surface potential (figure 3-1, picture 3-2).

The deep channels depth ranges from 1μm (with AZ 5214) to 10μm (with SU-8 10). The filter region depths range from 220nm to as little as 120nm. We hoped this depth would be enough to see some effects of the increase of the Debye layer thickness.

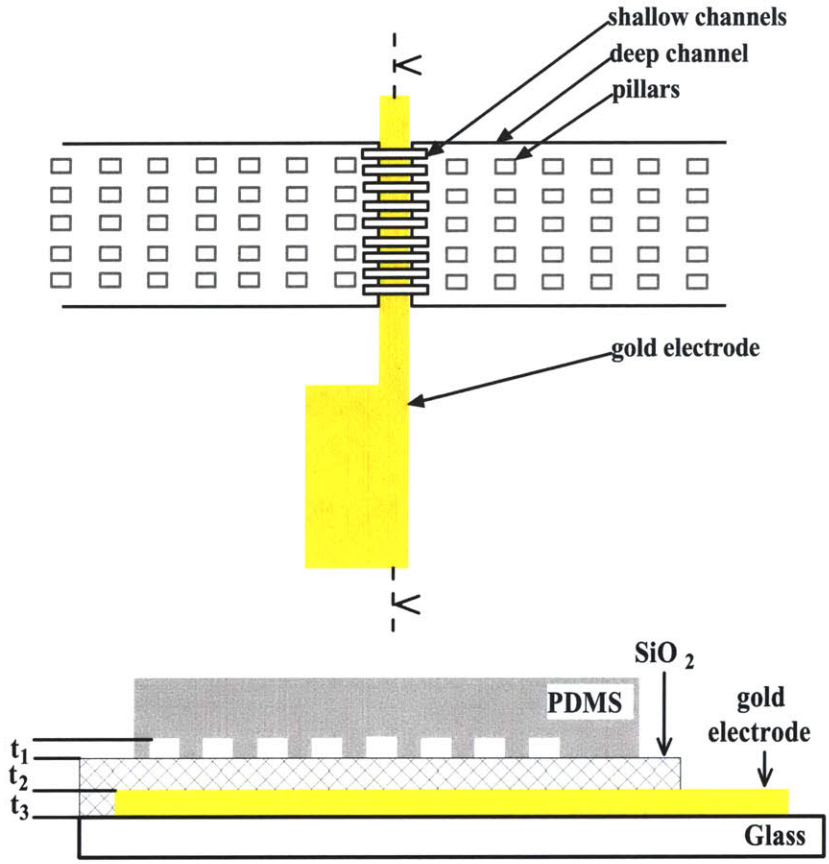

Figure 3-1: Top view (top image) and cross-section view (bottom image) of the filter region of the PDMS device. The thicknesses featured in the cross-section are t_1=120nm, t_2=250nm, t_3=130nm.

We want to study the effect of this hinderance of a fraction of the channel volume by the Debye layer on the flow of charged particles.

Please refer to Appendix A for the fabrication process flow of the silicon master, of the PDMS chips and of the gold electrodes on a glass substrate.

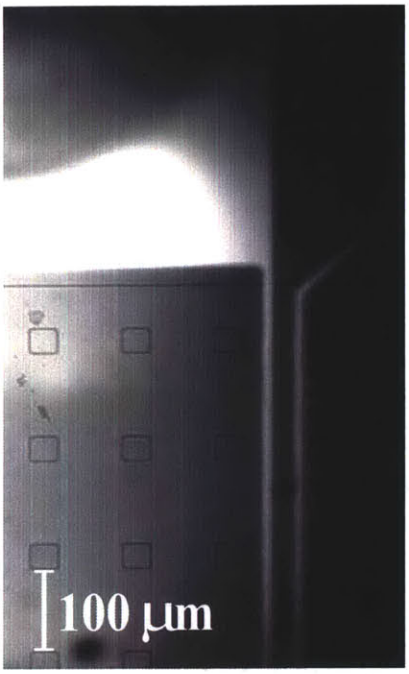

Figure 3-2: Top-view picture of the PDMS device showing the mesh of pillars, the shallow gates and the electrode underneath.

3.2 Experimental setup

3.2.1 Properties of the sample and buffer solutions

λ -DNA

λ-DNA was purchased from New England Biolabs (Beverly, MA). When DNA strands don't undergo any outside force, it forms a blob whose diameter between 500nm and 1.4μm depending on buffer, buffer concentration. Close to the depth our deep channels: 1.5μm.

Nanospheres

The nanospheres we used were green fluorescent, and negatively charged at pH $\simeq$ 9. They had diameters of 40-65nm for some experiments and 250nm for others.

Green Fluorescent Proteins

Recombinant GFP Protein 100μg is purchased from BD Bioscience Clontech. The GFP chromophore consists of a cyclic tripeptide derived from Ser-Tyr-Gly (amino acids 65-67) in the primary protein sequence (Cody et al., 1993) and is only fluorescent when embedded within the complete GFP protein ([38]). Its excitation band picks at 480nm and its emission band is centered on the 510nm wavelength.

TBE buffer

TBE buffer is a common buffer for DNA molecules. The one we used was purchased as powder from Sigma Aldrich (Saint Louis, Mo). TBE stands for Tris-Borate-EDTA buffer. After dilution with the indicated amount of water, the buffer has a 5X concentration: 0.445M Tris-Borate, 10mMEDTA, pH=8.3.

Phosphate buffer

Phosphate buffer is used to dissolve GFP. The phosphate buffer consists of phosphoric acid (H_3PO_4) in equilibrium with dihydrogen phosphate ion ($H_2PO_4^-$) and H^+. The pK for the phosphate buffer is depends on the constituting mix as shown in table 3.2.1. The phosphate buffer we used had pH 6.7.

pH	[NaOH]	[KH_2PO_4]
6.64	2.5mM	7.5mM
7.21	4.5mM	7.5mM
8.49	3.0mM	3.75mM

Table 3.1: Chemicals mix to make phosphate buffer and the resulting pH of the solution.

3.2.2 Microscope for fluorescence measurements

In order to track the concentration of the sample solution, we used dyed sample. For example DNA strands are dyed with YOYO-1 dye[1]. This dye's absorption wavelength

[1]YOYO-1 from the TOTO series of Dimeric Cyanine Nucleic Acid Stains of Molecular Probes.

is 491nm and its emission wavelength is 509nm. We chose the excitation filter, the dichroic mirror and the emission filter accordingly. The excitation and emission filters are band-passes that should allow respectively 491nm wavelengths and 509nm wavelengths to pass through. Ideally they would be as tight as possible. The dichroic's mirror function, as shown on figure 3-4, is to reflect the incoming excitation light (low transmittance) and to allow the light coming from the sample to go through (high transmittance).

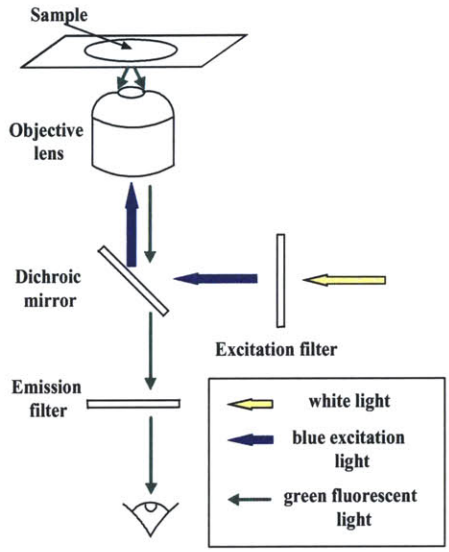

Figure 3-3: Microscope's filters setup.

The images are then captured with a thermoelectrically cooled CCD camera (Sensicam, Cooke Co.) and processed using IPLab software.

3.2.3 Electrical setup

One reservoir is cut in PDMS at each end of the deep channel. A platinum electrode is inserted in each of them, so as to create a potential difference of a few volts that will induce an electrophoretic flow of λ-DNA molecules in TBE buffer.
The potential imposed on the gold electrode can reach 100V.

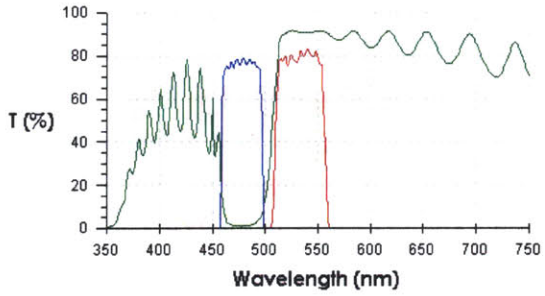

Figure 3-4: Microscope's filters transmittance plots. Blue: exciter; red: emitter; green: dichroic mirror.

3.3 Results

3.3.1 Flow reversion

We could observe a change in the direction of the flow as the potential applied on the electrode was going from positive ($V_{electrode} = 20V$) to very negative ($V_{electrode} = -100V$).

Nonetheless flow rate measurements proved very difficult for three reasons. First, the voltages required to reverse the flow systematically created bubbles. Second, the electrode fabrication was such that the surface bounded to the PDMS chip was not perfectly flat. Resulting in the frequent leaks along the electrode patterns. Finally, the insulating layer that we used didn't resist well to high voltages and was becoming conductive faster than we expected theoretically.

3.3.2 Ion selectivity

No selectivity of ions could be observed, however low the potential applied on the electrode. The depth of the shallow region was probably too large for the change in thickness of the Debye layer to have any significant effect. (The depth of the shallow region had been determined to suit a previous Coulter counter experiment).

Chapter 4

Characterization of nanofluidic preconcentrator

Due to the difficulties in reaching very small depths with PDMS nanochannel, the predicted effect of ion selectivity could not be observed in the previous chapter. Therefore, it was decided to use the nanofluidic preconcentrator made by more reliable silicon nanochannel fabrication technique ([39]) to study the effect of gate potential control. In this chapter, we will characterize the operation of nanofluidic preconcentrator without gate potential control, as a baseline for the comparison in later chapters.

Silicon devices allow us to fabricate thinner filters (depth down to 20nm) ([37]), more reliable devices that don't develop leaks, and to use more resistant dielectric layers.

4.1 Design and working principle

Please see the description of the device above in paragraph 2.2.4.

4.2 Fabrication

The fabrication process used to make this device is similar to the original planar nanochannel fabrication technique by Han et al.([39]). The feasibility of this technique to fabricate nanocannels as thin as 20nm has been demonstrated by Mao et al. ([40]) recently.

Please consult Appendix B for the fabrication process flow of the silicon device.

4.3 Experimental setup

4.3.1 Properties of the sample and buffer solutions

The buffer and sample solutions are the same as the ones described above 3.2.1.

4.3.2 Microscope for fluorescence measurements

The microscope setup used for fluorescence measurements is the same as the one described above 3.2.2.

4.3.3 Electrical setup

To impose the voltages, we use two high voltage power supplies (Model PS325/2500V-25W from Stanford Research Systems, Inc). A home-made voltage divider was used to distribute and control the potential applied to the reservoirs. Platinum wires to make the connection between the coper wires and the solution.

4.4 An experimental issue: flushing

One of the experimental issues we are faced with in the nanofluidic experiments we will describe is flushing. Suppose we wish to change buffer from one set of experiments to the next. Assume we substitute a buffer with concentration c_1 with the same buffer

at concentration c_2. Our concern is to have a buffer at concentration precisely c_2 when we start our new set of experiments, and not a concentration in between c_1 and c_2. That is why we wish to flush the previous buffer out of the channels as completely as possible.

Two mechanisms help reach our goal of working with a pure, homogeneous solution at the desired concentration:

- One is diffusion inside the reservoir. Because of the intricate geometry of the reservoir, some solution remains trapped in areas of the reservoir that cannot be reached using a pipette. Let's evaluate this volume. For 650μm thick wafer, and a square reservoir dug into it with an angle of 45° and side 2mm (figure 4-1), this volume is

$$V_{left-over} \simeq 4 \cdot \frac{1}{2} \cdot 2 \times 10^{-3} \cdot (6.5 \times 10^{-4})^2 \simeq 1.7\mu L$$

  This volume of leftover solution will diffuse into the new solution (around $100\mu L$) without noticeably alterating it.

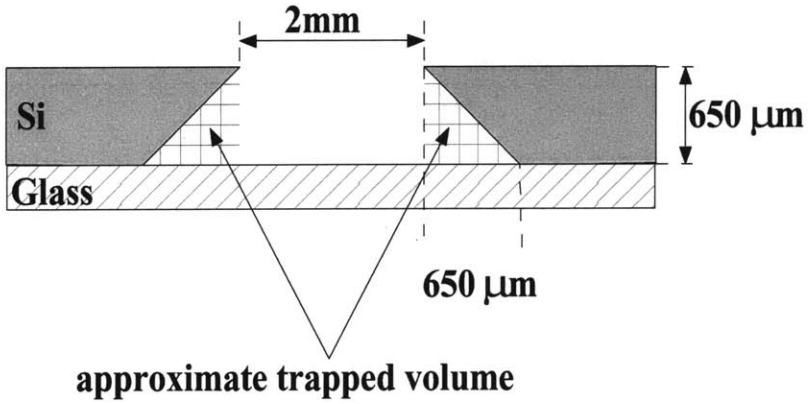

Figure 4-1: Cross-section of the reservoir. Volume of solution that cannot be reached when the reservoir is emptied with a pipette is represented by the texture of orthogonal lines.

- Flow rate in a channel with rectangular section. Call w its width and h its depth,

such that w is much greater than h. Then the flow rate F can be calculated:

$$\begin{aligned} F &= \frac{\Delta P w h^3}{12\eta L} \\ F &\simeq \frac{5 \times 10^4 \cdot 10^{-5} \cdot (1 \times 10^{-6})^3}{12 \cdot 10^{-3} \cdot 10^{-2}} \\ F &\simeq 5pL.s^{-1} \end{aligned}$$

This gives us an order of magnitude of the flow rate we can expect. Given that we wish to flush a several times the volume contained in the nanochannel

$$V_{channel} \simeq 3 \times 10^{-2} \cdot 10^{-5} \cdot 1.5 \times 10^{-6} \simeq 0.5nL.$$

The time dedicated to flushing the volume contained in the channel is then

$$\frac{V_{channel}}{F} \simeq \frac{5 \times 10^{-10}}{5 \times 10^{-12}} \simeq 30sec.$$

In practice we multiply this time by a factor 20 to ensure proper flushing.

4.5 Concentration experiments performed on a λ-DNA sample solution

4.5.1 Control of λ-DNA flow through the gate

In the experimental conditions described above, the effect of electrophoresis dominates that of the electroosmotic flow on λ-DNA molecules. We chose the voltages applied to the reservoir to drive the λ-DNA through the nanochannels. The DNA can either flow freely through the gates, or find itself unable to go through the gates depending on the buffer concentrations. At lower buffer concentrations, ion currents through the nanochannel will generate concentration polarization near the nanochannel entrance, which hinders the DNA transport through the nanocannel. We try to alter this behavior by applying an external voltage V_{gate}. If initially the DNA can freely flow

through the gate, then we will try to decrease V_{gate}, so as to increase the double layer thickness, create a charge polarization and a depletion region that would prevent the DNA molecules from flowing through. This is what we refer to as '**blocking**' in the table below (4.5.1). Reversely, if at a different buffer concentration, the DNA cannot flow through the gate, then by increasing V_{gate}, we will make the double layer thickness negligible and consequently facilitate the transfer of ions through the nanochannels. This is what we refer to as '**allowing**' in the table below.

TBE concentation	nanochannel depth 42nm
0.89M (10X)	unhindered
0.44M (5X)	unhindered
3.6×10^{-1}M (4X)	unhindered
2.7×10^{-1}M (3X)	unhindered but 'blocking' for V_{gate}=-100V
1.8×10^{-1}M (2X)	unhindered
8.9×10^{-2}M (1X)	hindered but 'allowing' for V_{gate}=60V
8.9×10^{-3}M (0.1X)	hindered
4.45×10^{-3}M (0.05X)	hindered

Table 4.1: Behavior of the DNA unhindered or hindered meaning the DNA respectively can and cannot flow through the nanochannels.

The pictures in figures 4-2 and 4-3 illustrate the content of the table 4.5.1.

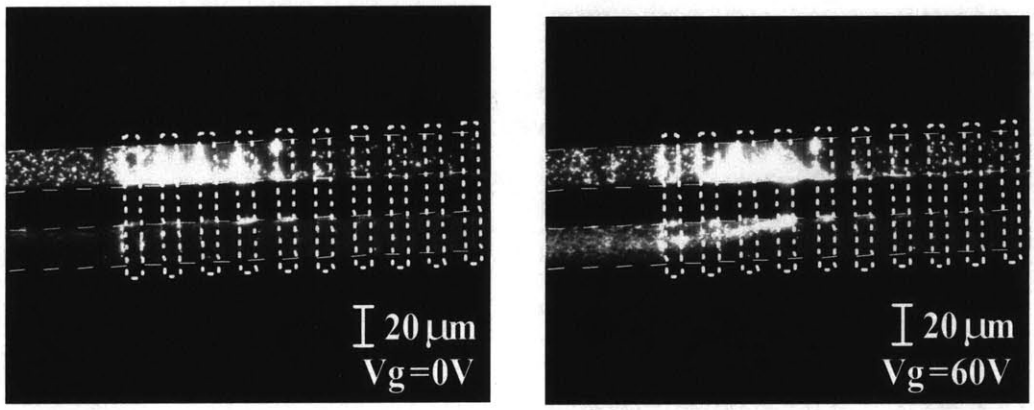

Figure 4-2: Effect of the gate potential on the flow of λ-DNA through the nanochannels. The concentration of the TBE buffer used is 8.9×10^{-2}M. Increasing the gate potential increases the flow of DNA from the top microchannel to the bottom microchannel through the nanochannels.

When the flow of DNA through the gate is hindered, plugs of DNA are forming at the entrance of the gate. This high-concentration DNA plug can then easily be flushed away by changing the applied voltages.
One should nonetheless acknowledge that a secondary effect combines with the double layer thickness to account for the observations we make: the electroosmotic flow rate is altered by the application of a voltage on the bulk silicon.

4.5.2 Transient behavior

As V_{gate} is changed from floated to a given voltage, we can observe a transient behavior. The DNA velocity is temporarily increased, before reaching a steady state.
This behavior is meaningful because it could be a hint that in certain conditions, the capacitance behavior of our device is not negligible.
This accelerated motion of charged molecules should translate into a spike in current intensity. So we decided to monitor the current intensity both for the actual device and for a control device. The experimental setup is described in figures 4-4 and 4-5. The sample solution is λ-DNA in 10X (ie. 0.89M Tris-Borate) TBE buffer.

The measured currents (figures 4-6 and 4-7) do display spikes when the potential V_{gate} goes from floated to a 15V, as well as when it goes from 15V to floated. The characteristic time constant is different for the actual device and for the control experiment: 30 seconds vs. 3 seconds. This experiment supports the capacitor model for the device introduced above (paragraph 2.2.2). The difference in time constants is due to the different geometries of the two devices. The control experiment proves that the capacitor behavior can take place simply with a dielectric layer between the conductive silicon and the conductive buffer solution.

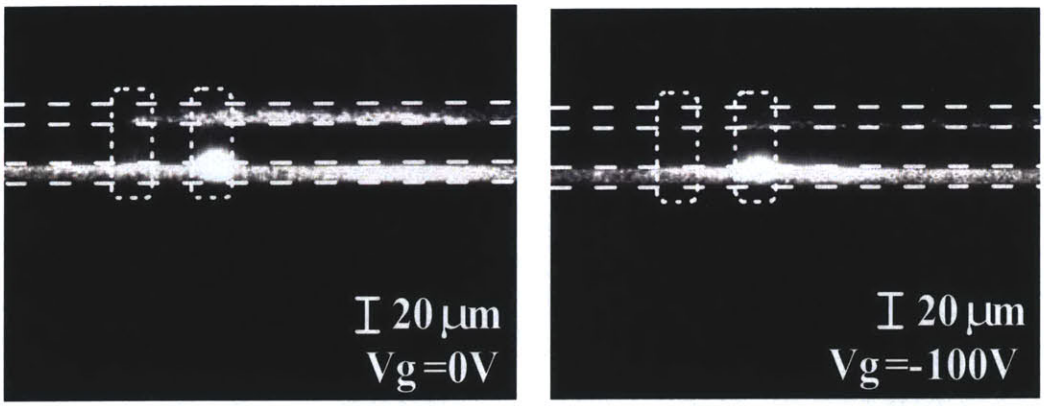

Figure 4-3: Effect of the gate potential on the flow of λ-DNA through the nanochannels. The concentration of the TBE buffer used is 2.7×10^{-1}M. Decreasing the gate potential hinders the flow of DNA from the bottom microchannel to the top microchannel through the nanochannels.

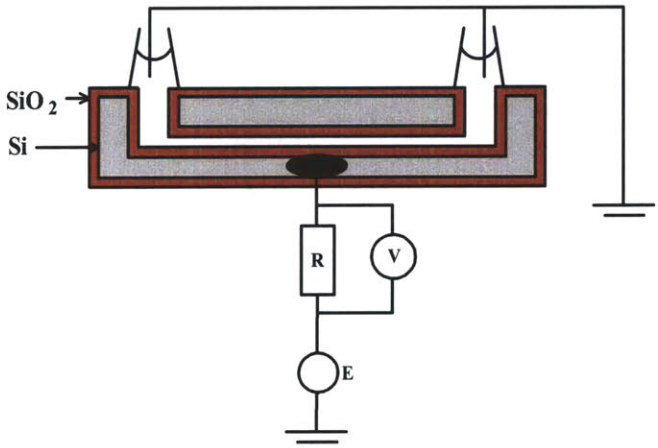

Figure 4-4: Setup for the measurement of the transient current. R=91kΩ and E is switched between floated and a set value. The solution used is TBE at concentration 8.9×10^{-2}M. The reservoirs R1, R3, R4 and R5 were grounded.

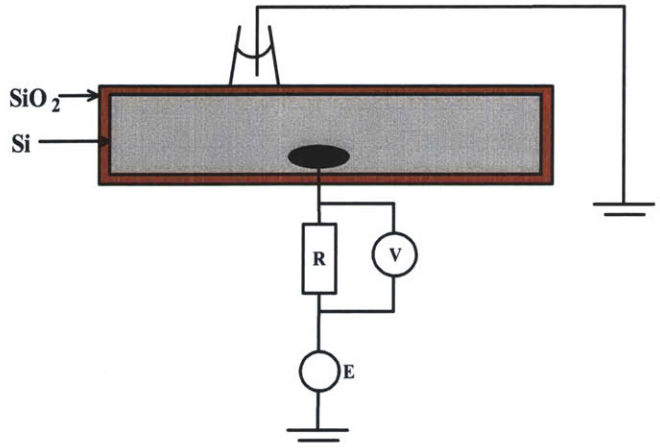

Figure 4-5: Control experiment setup for the measurement of the transient current.R=91kΩ and E is switched between floated and a set value. The solution used is TBE at concentration 8.9×10^{-2}M. The one reservoir glued on top of the silicon wafer was grounded. The process for the creation of this control device was identical to that for the concentrator. Consequently the oxide layer thicknesses are identical (500nm).

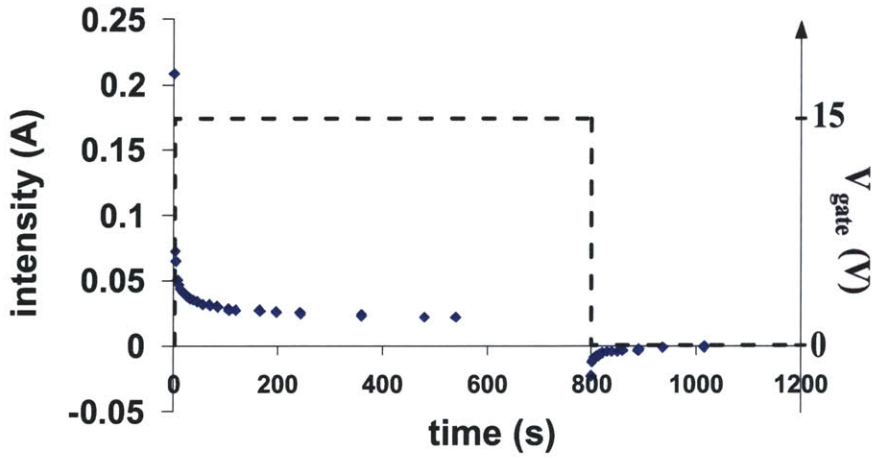

Figure 4-6: Measured current intensity through the setup of figure 4-4 as V_{gate} is changed.

4.6 Pre-concentration of GFP

4.6.1 Experimental setup

We use a solution of GFP at a concentration of 33μM in phosphate buffer with concentration 1mM. The electrical potentials applied are described in figure 4-8.

4.6.2 Results

The conditions described above are maintained for a certain amount of time, during which, at regular intervals we take intensity measurements to follow the increase in concentration in GFP plug. The result is displayed in picture 4-9. Figure 4-10 shows the rate at which the protein concentration takes place in one example of experimental conditions. The series of images 4-11 pictures the evolution of the plug between the initial state and 3 minutes.

Here we repeat the same experimental conditions at 3 different moments of the life of the silicon device. The first experiment is conducted on a new device. The second series of data is taken as the device is 12hours old, and the last series as the

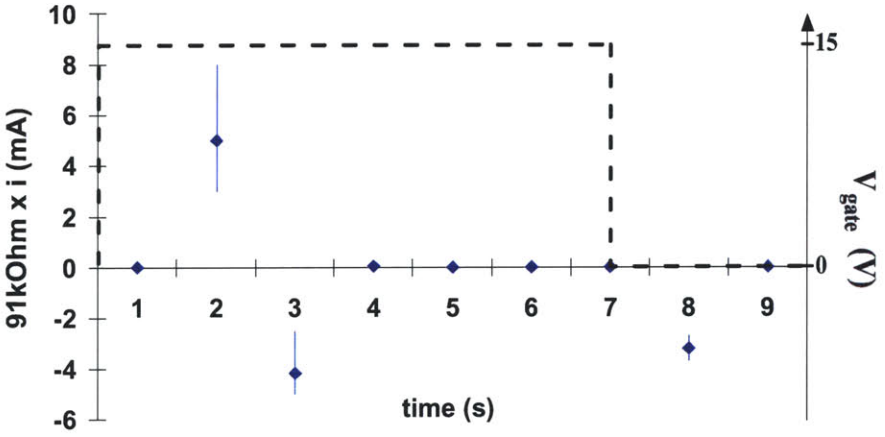

Figure 4-7: Control experiment measurement of the current intensity a the device described in figure 4-5 as V_{gate} is changed.

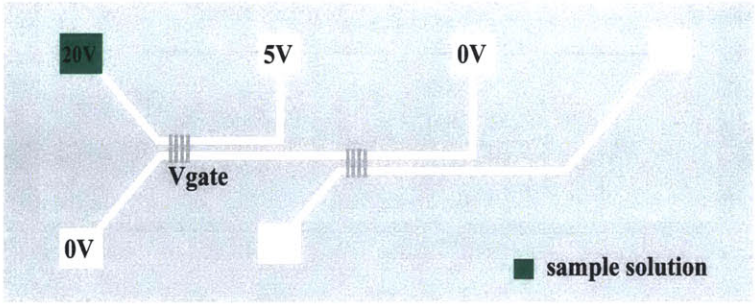

Figure 4-8: Experimental conditions leading to the formation of a plug

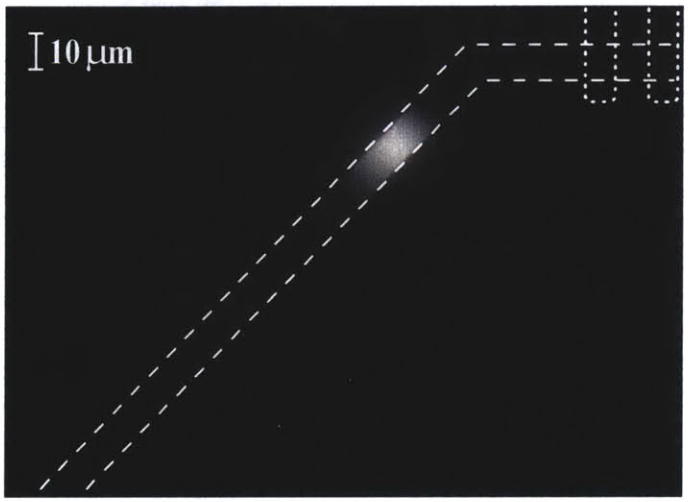

Figure 4-9: Picture of a GFP plug at the boundary of a depletion region, in the channel of a silicon device. The plug is formed using an electrokinetic flow. The dashed line represents the contour of the 1.5μm-deep channel, and the dotted line represents the contour of the 62nm-deep nanochannels.

device has already been used for 2 consecutive days. The results are plotted in figure 4-12.

4.6.3 Interpretation

It has already be shown that nanochannels with depth of the order of the tens of nanometers can function as permselective exchange membranes ([14, 15]). The **concentration polarization** mechanism at work and its three regimes have been previ-

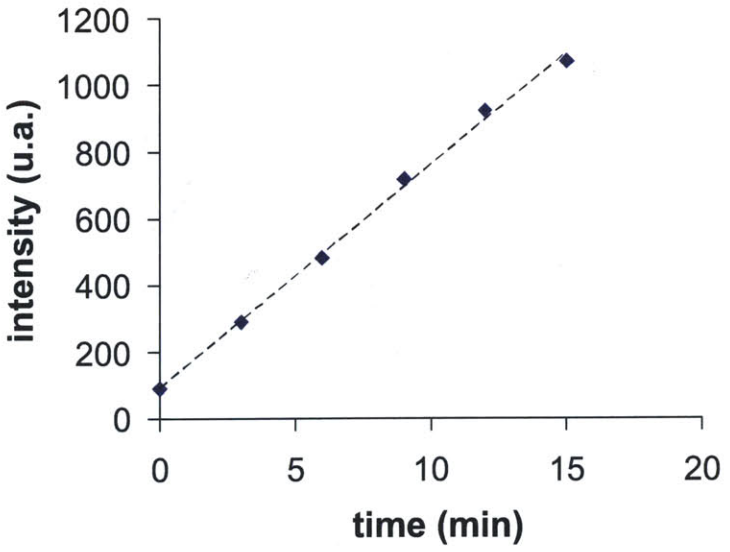

Figure 4-10: GFP plug formation rate. For this experiments V5=20V, V3=5V, V1=V2=0V and V_{gate}=5V.

ously studied ([41–43]). 'The passing of current through ideally selective membranes is exclusively determined by counter-ions because inside such membranes co-ions are absent. A bulk charge appears at the side where counter-ions enter it from the bulk of the electrolyte. The co-ions move in the opposite direction, away from the membrane. This leads to co-ions depletion at this side of the membrane. In turn this leads to a diffusion flow from the electrolyte to the membrane surface. As there is no co-ion flow inside the membrane, this implies that in every point of the diffuse and diffusion layer eletromigration and diffuzion of co-ions are exactly balanced ([44]).' In the depleted charge polarization zone, the combination of electroosmotic flow, diffusion, electromigration creates the convective-diffusion layer with reduced ionic concentrations. In our case, the nanochannels are at least partly hindered by double layers that make the flux of counter-ions through them larger than the flux of co-ions, if not perfectly charge selective. GFP are co-ions in this system and both driven towards the gate by an EOF flow, and prevented to enter the gate by the concentration polarization zone. The concentration of co-ions can be attributed to the combination of the driv-

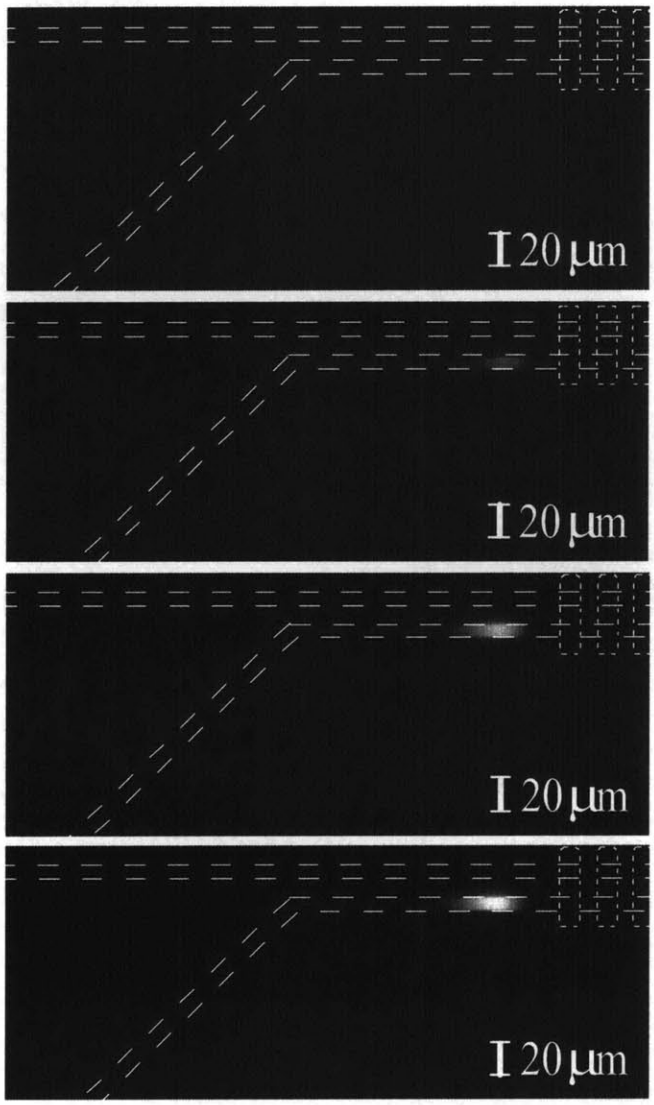

Figure 4-11: Plug formed under the conditions described in paragraph 4-8 after respectively 0minutes, 2minutes, 2minutes 30seconds and 3minutes for the top, second, third and bottom pictures.

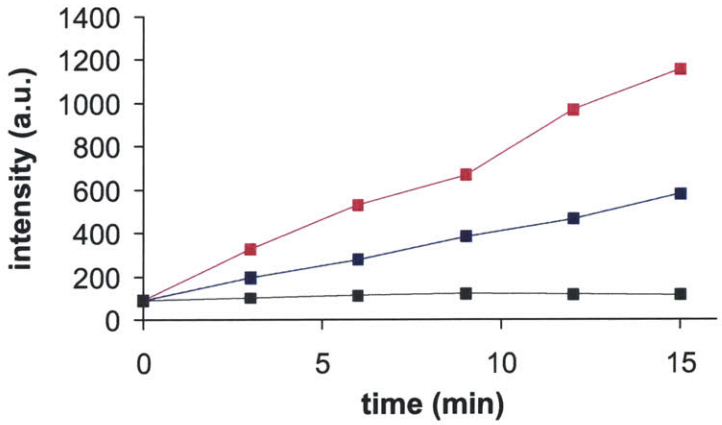

Figure 4-12: Decay of the plug formation rate with time. Pink line: new device; blue line: 12hours old device; green line: 2days old device. For this experiments V5=20V, V3=5V, V1=V2=0V and V_{gate}=-10V.

ing electric field and the stacking at the boundary of the ion depletion region ([21]).

The constitution of a polarized double layer, in turn modifies the electroosmosis. We say that electroosmosis of the second kind is taking place. 'The polarization of the double layer and the appearance of the space charge layer change the pressure near the membrane, leading to the appearance of a velocity component related to this pressure that is absent in the Smoluckowski equation ([45])'. The imbalance between counter-ions and co-ions in the depletion region creates a local space charge that is responsible of the electroosmosis of the second kind ([46]). So called by opposition to the electroosmosis of the first kind that is due to the local space charge in the double layer (paragraph 2.1.2). Under a strong enough electric fields, the electrophoretic and electroosmotic flows of the second kind are one or two orders of magnitude greater than the flows predicted by the Schmoluchowsky's equations. That is why we measured the flow rate, further in the thesis. High flow rates are a signature of electroosmosis of the second kind, and would simultaneously be an additional indication of the presence of charge polarization.

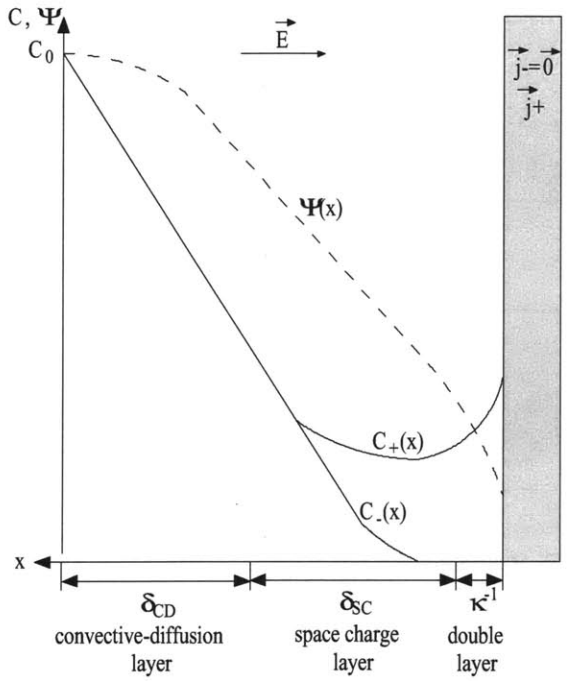

Figure 4-13: Schematic representation of co-ions and counter-ions concentrations and electrical potential $\Psi(x)$. Adapted from 'Advances in Colloid and Interface Science' by P. Taylor, publisher Elsevier Science Publishers B.V.

Figure 4-14 shows the localizations of the concentration plug, of the space charge layer and of the double layers.

Concerning the decay in the second experimental results presented above, we attribute it to **non-specific binding** on the channel walls. This adsorption could be the cause of the reduction in the efficiency of the pre-concentration mechanism.

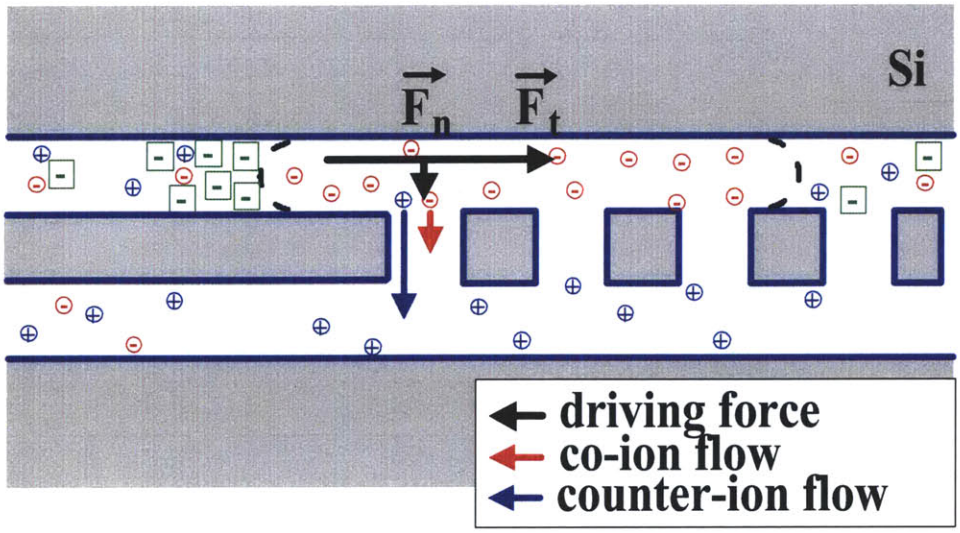

Figure 4-14: Schematic representation of the space charge layer. Blue circled '+' signs and thick blue lines represent the buffer counter-ions. Red circled '-' signs represent the buffer co-ions. Green '-' signs in green squares represent the co-ions of the sample solution. The black arrow symbolizes the driving mechanism that wants to force the buffer and sample solution through the nanochannels and along the deep channel. Depending on the position in the channel, the ratio of the components of this force normal and tangential to the nanochannels entrance varies. This driving force is that exerted by an electric field on a charged particle in this chapter. In chapter 6 it is a pressure-induced force. The section between dotted curved lines is the space charge layer. The sample molecules plug whose intensity is measured in the following chapters is featured in the figure by the higher density of green squares.

4.7 Modification of depletion region width with the buffer ionic strength

4.7.1 Experimental setup

In this section we will measure the width of the depletion region as a function of the buffer ionic strength. The protein solutions used are GFP samples of concentration 11μM in phosphate buffer solution with successive concentrations 2.5mM, 1mM, 0.3mM and 0.1mM. The gate voltage is set at V_{gate}=0V for all experiments. The potentials applied in the reservoirs are indicated in figure 4-15.

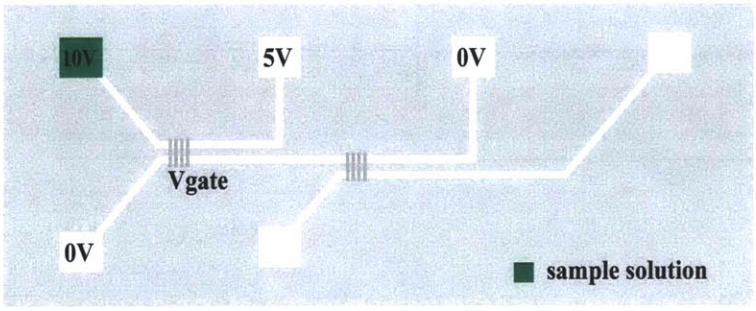

Figure 4-15: Experimental conditions for the measurement of the width of the depletion region.

4.7.2 Results

The series of pictures 4-17 shows the plug in the channel. The nanochannels cannot be seen on the screen shots. They would be at the right of the right boundary of the pictures.

4.7.3 Interpretation

A higher buffer ionic strength corresponds to a higher buffer concentration. If the same electric fields are imposed, and the system is the same in all experiments, we expect the ionic currents resulting from the permselectivity of the nanochannels will

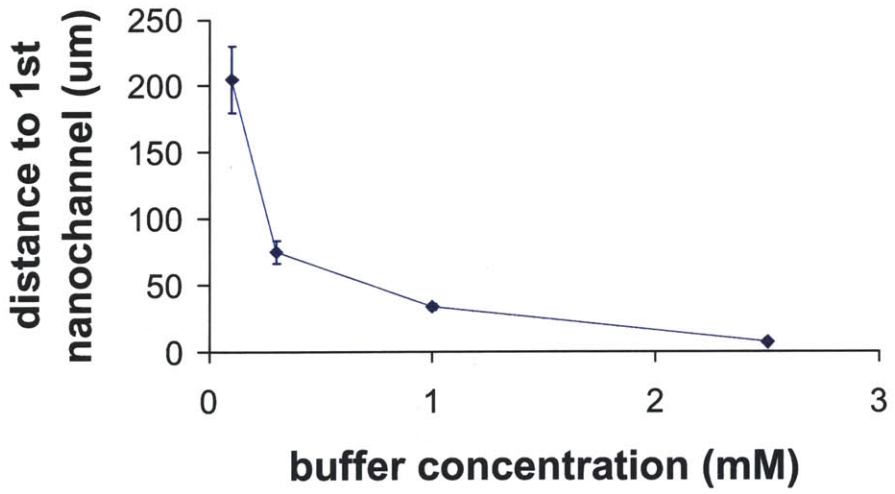

Figure 4-16: Position of the concentration plug as a function of the phosphate buffer concentration.

be comparable, ie. as many counter-ions and co-ions are expected to be in excess on each side of the nanochannels for all experiments. For this given number of ions, the higher the buffer concentration, the smaller the volume needed to create the ion depletion region. It is what is observed experimentally.

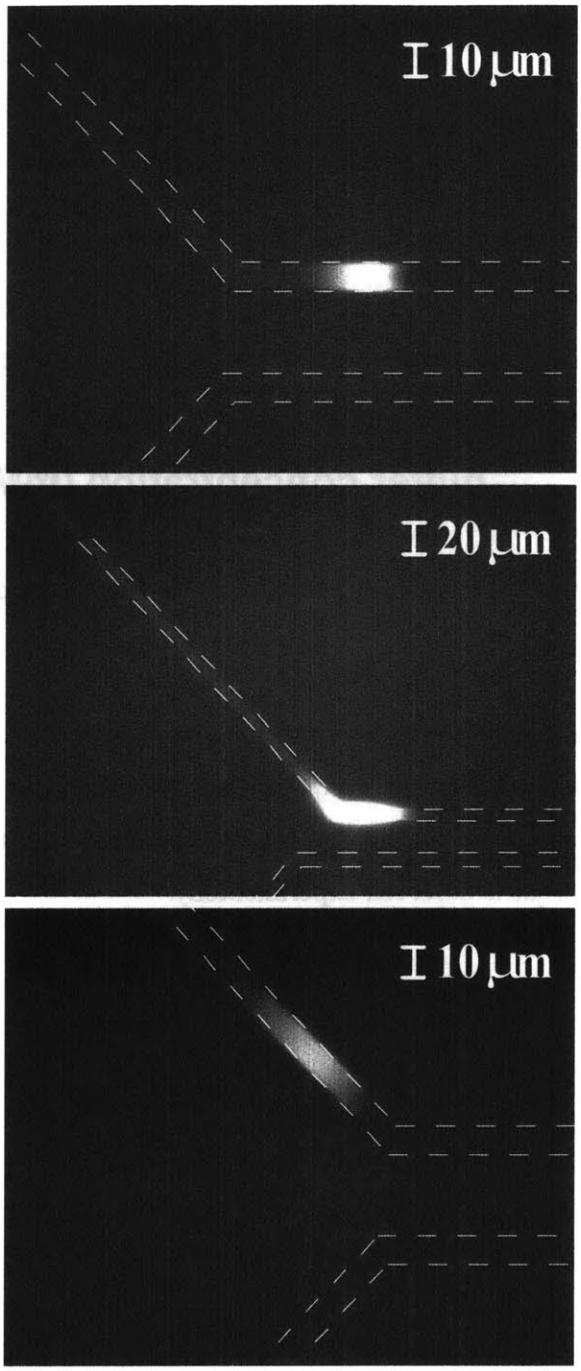

Figure 4-17: Position of the GFP plug in several phosphate buffer concentrations. The respective concentrations are for the top picture: 2.5mM; for the middle picture: 1mM; for the bottom picture: 0.3mM.

Chapter 5

External gate potential control of pre-concentration

In this chapter, we will attempt to modulate the operation efficiency of the nanofluidic preconcentrator by changing the gate potential of the silicon substrate. Controlling the gate potential modulates the zeta potential of the nanofluidic channel, which leads to real-time control of nanofluidic concentration efficiency.

5.1 Modification of the depletion region width with V_{gate}

5.1.1 Experimental conditions

This experiment is done with a GFP solution ($c = 3.3\mu M$) in phosphate buffer (c=1mM). A potential difference (10V to 5V) is applied at the end of the channel initially containing the sample GFP, so as to drive it from one reservoir to the other. The two reservoirs at the end of the channel connected to the previous one by nanochannels are grounded. This second potential difference is the one responsible for the existence of the permselectivity described above (paragraph 4.6.3).

We measured the distance between the center of mass of the plug and the center of the nanochannel closest to the reservoir where the fluorescent sample was loaded.

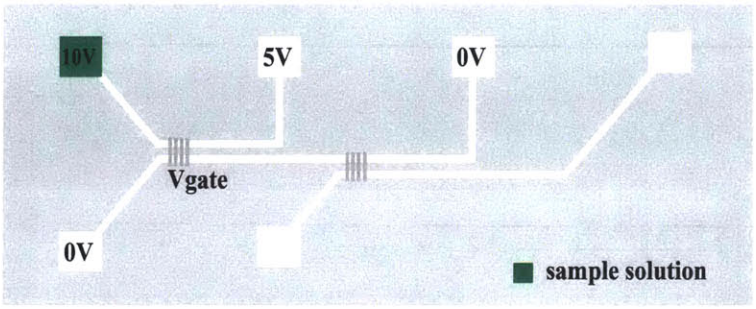

Figure 5-1: Experimental conditions for the measurement of the position of GFP concentration plug as a function of Vgate

The center of mass of the plug was approximated as the middle point between the leftmost and rightmost edges of the plug that corresponded to a certain intensity level. If the plug is between the reservoir with the fluorescent sample and the nanochannel, the distance is counted as positive. If the plug is beyond the first nanochannel, it is counted as negative (figure 5-2).

All other parameters being kept constant, we changed Vgate and we measured this arithmetic distance between the plug and the first nanochannel.

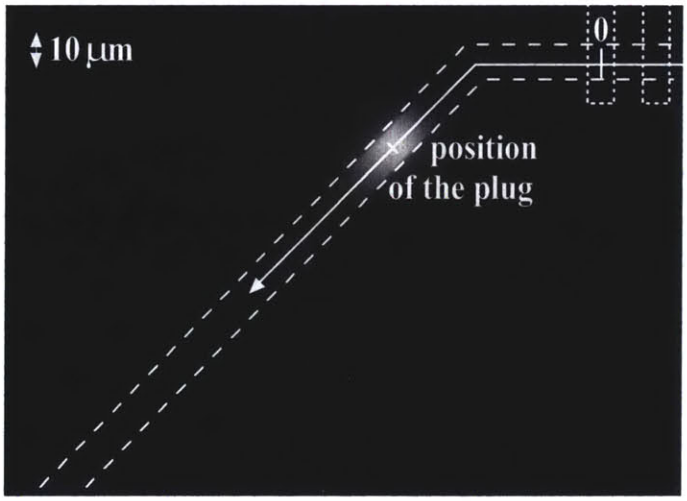

Figure 5-2: The arithmetic distance between the GFP plug position and the first nanochannel is measured along the axis represented by the full white line.

5.1.2 Results

We notice on figure 5-3 an almost linear relationship between the gate voltage and the distance between the plug and the nanochannel.

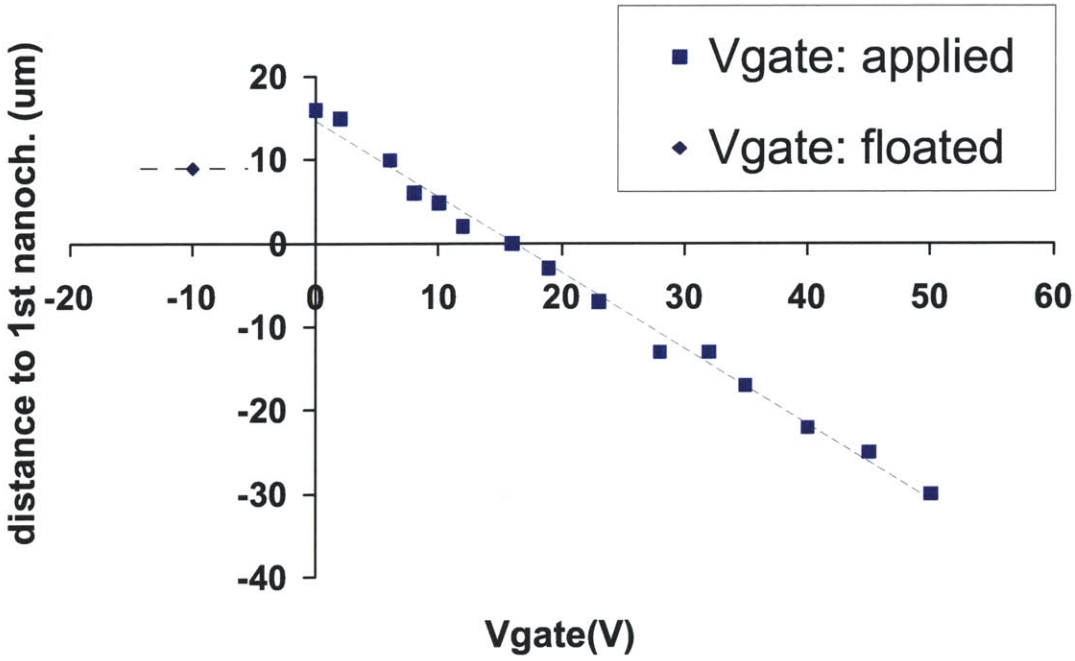

Figure 5-3: Position of the plug as a function of Vgate. The linear fit grants $R^2 = .992$ and $d_1 = -0.9 \times V_{gate} + 14.6$

We can also notice that the position of the plug when the gate is floated, corresponds to a voltage gate V_{gate} greater than 6V and smaller than 8V. And indeed, given the voltages imposed (5-1), we expect V_{gate} to be i the 5V to 10V range, and most likely between 7V and 8V given the geometry of the channel.

5.1.3 Interpretation

Numerical simulations ([35]) showed that when the thickness of a channel is becoming comparable to the Debye length, then the co-ions are excluded from the channel. The same authors showed that the higher the absolute value of the surface charge, the

stronger the counter-ion current was through the gate. Coupling these results with the concentration polarization, we can explain the fact that the plug moves away from the nanochannels as V_{gate} is decreased by an increased flow of counter-ions through the nanochannels, leading to a stronger charge polarization and consequently to a wider concentration polarization zone. The GFP, being a co-ion, is trapped at the outside boundary of this concentration polarization zone. When this zone grows wider, the GFP plug is pushed away from the nanochannels.

5.2 Influence of V_{gate} on the pre-concentration rate

5.2.1 Experimental conditions

This experiment is made with the same solution as above (5-1), ie a GFP solution ($c = 3.3\mu M$) in phosphate buffer (c=1mM). The potentials applied are given in figure 5-4.

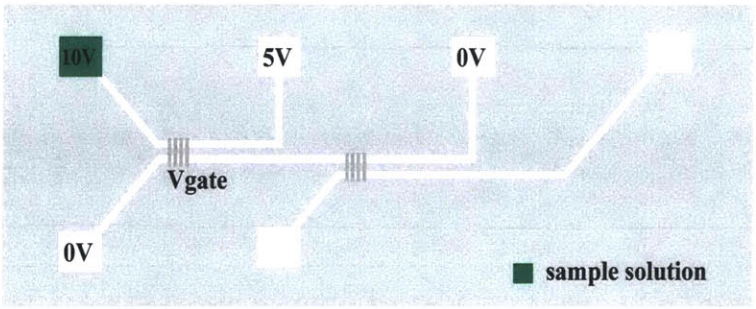

Figure 5-4: Experimental setup for the pre-concentration rate measurement

Because of the fast alteration of the surface conditions, we can only make rigorous comparisons over short period of time. That is why we compared first values of V_{gate} negative or null and later in a separate experiment, values of V_{gate} positive or null.

The 'intensity' measurement featured the y-axes of the plots corresponds to the measurement of the maximum fluorescence intensity in the plug.

5.2.2 Results

We can clearly see from the plots 5-5 and 5-6 that the lower V_{gate}, the faster the concentration rate.

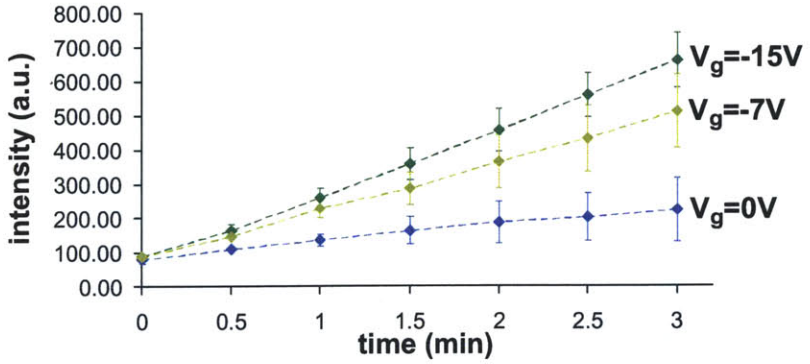

Figure 5-5: Comparison of the preconcentration rates for V_{gate}=0V, 15V and 30V.

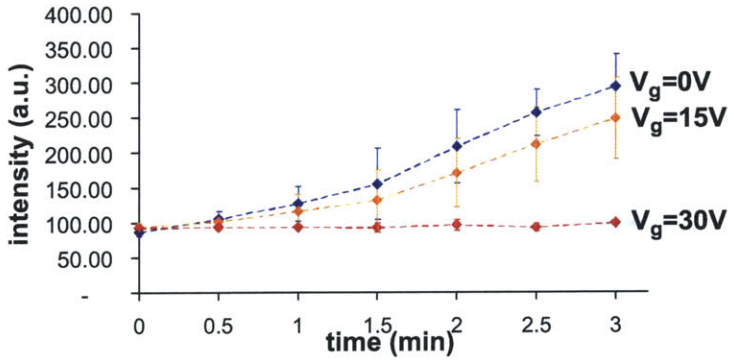

Figure 5-6: Comparison of the preconcentration rates for V_{gate}=0V, -7V and -15V.

The following series of pictures (pictures 5-7 shows electrokinetic plugs formed for different values of V_{gate}.

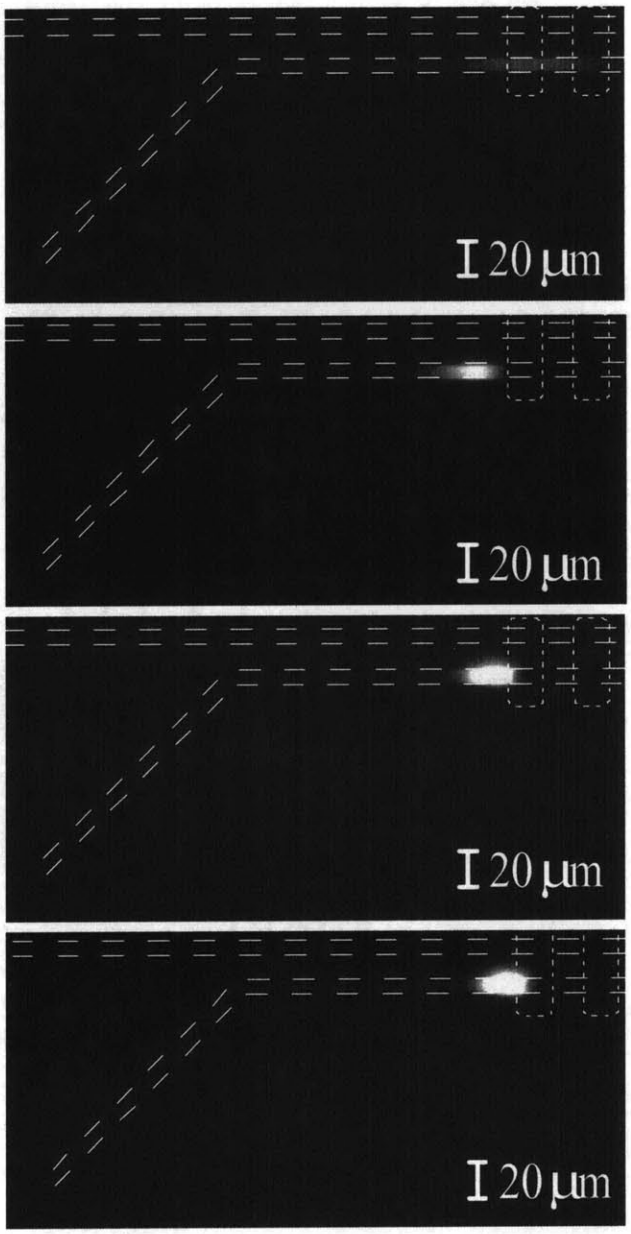

Figure 5-7: Plug formed under the conditions described in paragraph 5.1.1 after 3 minutes with V_{gate} set respectively to 30V, 0V, -7V and -15V for the top, second, third and bottom pictures.

5.2.3 Interpretation

We can interpret this trend by noting that the lower the gate voltage, the wider the double layer in the nanochannels. And then the wider the double layer, the more efficient the charge selectivity ([35]). This difference in transport numbers of co-ions and counter-ions creates charge polarization zones. One depleted and one concentrated respectively at the cathodic and anodic sides of the nanochannels. So when V_{gate} is decreased, the nanochannel becomes more permselective and the plug forms faster.

5.3 Electroosmosis of the second kind

5.3.1 Experimental conditions

In this experiment, we will try to detect the presence of electroosmosis of the second kind by a flow rate measurement. The sample solution used is a green fluorescent nanospheres solution (Duke Scientific Corp., CAT. NO. G250, diameter 250nm) diluted 500 in a phosphate buffer solution of concentration 1mM.

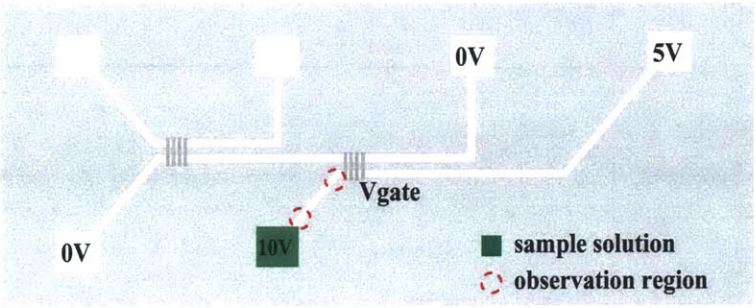

Figure 5-8: Experimental setup for the flow rate measurement experiment. The sample is loaded in the green reservoir. If a voltage is applied at a point of the device, it is written on the figure. No voltage indication means this point is floated.

The velocity of the nanospheres is calculated by taking a movie of their motion with the CCD camera. We measure their displacement between two frames of the movie and divide by the time interval between two frames to obtain their individ-

ual speeds. This measurement is made at two points of the channel: close to the nanochannels and close to the exit of the reservoir (figure 5-8).

5.3.2 Results

The surface potential on the channel walls influences the flow rate. The average velocities and their standard deviations are calculated on samples of size around 10.

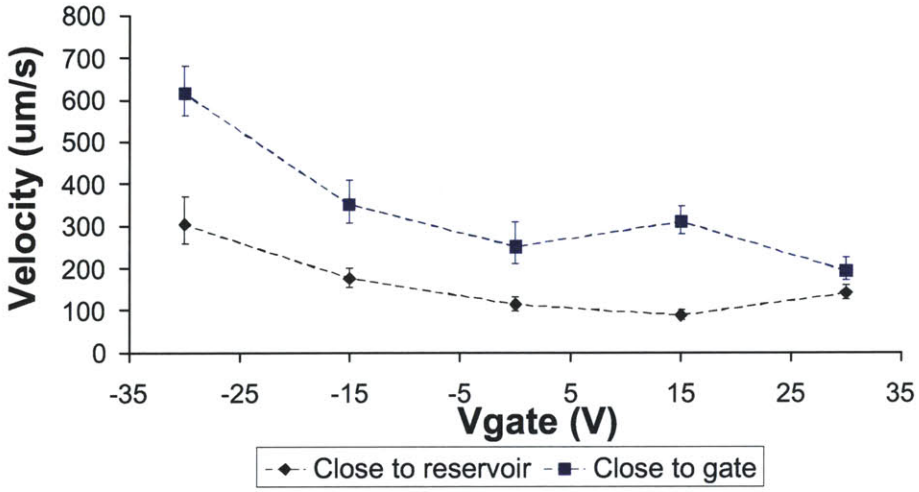

Figure 5-9: Measurement of the celerity of the nanospheres as function of V_{gate}.

5.3.3 Interpretation

This experience was aimed at detecting the presence of electroosmosis of the second kind. One of its characteristic traces being an increased flow rate as a 'pressure component', due to the space charge layer, reinforces the regular electroosmosis. The increased flow rate that we observe as V_{gate} is decreased can nonetheless be attributed as well to the regular electroosmosis as to the electroosmosis of the second kind.

Chapter 6

Characterization of pressure-induced concentration polarization in nanofluidic channels

In this chapter, we explore another unique nanofluidic phenomenon using the same nanofluidic device used in the previous chapter. Due to non-negligible Debye layer in nanofluidic channel, fluid flow through nanochannel, as well as ion current, will generate charge separation across the channel. As a result, a pressure-driven flow through the nanochannel generates concentration polarization behaviors similar to the ones described in the previous chapter. We will characterize this phenomena in this chapter.

6.1 Device

The device used for this set of experiments is the same as the one used in the previous chapter. Please see the description of the device above in paragraph 2.2.4.

6.2 Experimental setup

6.2.1 Solutions, fluorescence measurement, electrical setting

Most of the experimental setup is left unchanged from the previous experiments. The buffer and sample solutions are the same as the ones described above 3.2.1. The microscope setup used for fluorescence measurements is the same as the one described in paragraph 3.2.2. To impose the voltages, we use the same two high voltage power supplies (Model PS325/2500V-25W from Stanford Research Systems, Inc). A voltage divider. Platinum wires to make the connection between the coper wires and the solution.

6.2.2 Pressure setup

From now on in this thesis, we will use pressure to drive the solution through the channels. The pressure will be created by the compression of the air enclosed in the 'system'. The system is comprised of the inside of a 30ml syringe, a 30cm long silicon tube, a pipette tip and the reservoir dug into the silicon wafer (figure 6-1). In order to apply pressures of the order of half an atmosphere, we need to conceive a setup hermetic enough. We choose the inner diameter of the silicone tubing small enough so the tube can hold on fast onto the pipette tips of the syringe and on the device. The watertightness between the pipette tip and the device is ensured by a generous application of epoxy glue.

We can evaluate the pressure that can be created assuming the air is a perfect gas, governed by the thermodynamic law:

$$PV = nRT$$

with P: pressure inside the system; V: volume of the system; n: number of moles of gas enclosed in the system; R: gas constant (8.314J$\cdot$ mol$^{-1}\cdot$ K^{-1}); T: temperature inside the system.

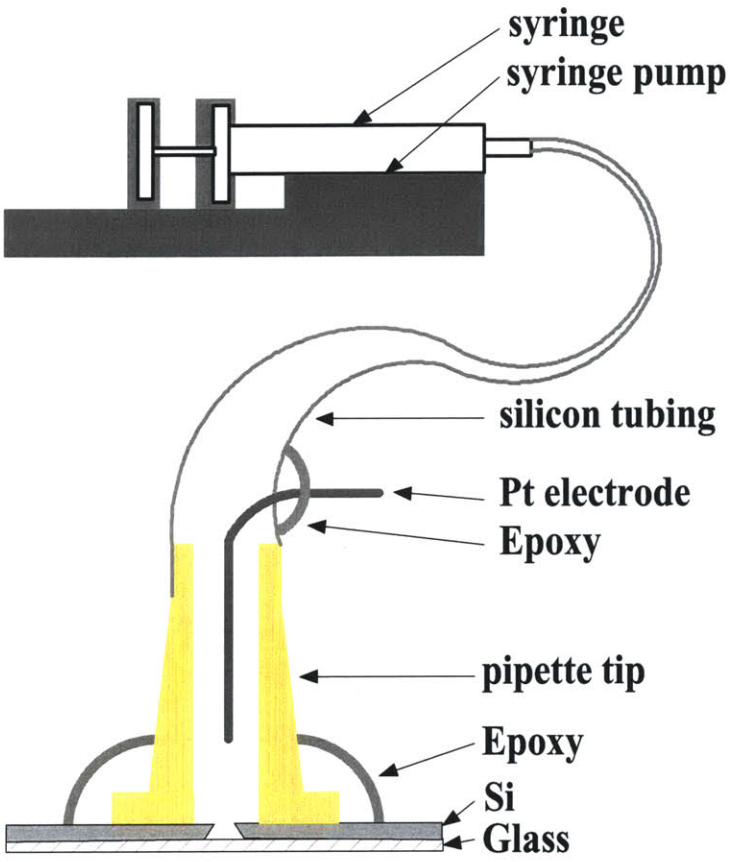

Figure 6-1: Experimental setup used to apply pressure on the solution contained in a reservoir.

Assuming the environment around the system is a heat sink imposing a temperature T, then the temperature of the system in all equilibrium states will be T. The subscript 'i' will designate the initial state, and the subscript 'f' the final state. Suppose force the inner volume of the syringe from 15ml to 10ml, then we have:

$$\begin{aligned}
P_i Vi &= P_f V_f \\
P_f &= P_i \times \frac{V_i}{V_f} \\
P_f &= P_i \times \frac{V_{i,syringe} + V_{i,tube} + V_{i,pipettetip}}{V_{f,syringe} + V_{f,tube} + V_{f,pipettetip}} \\
P_f &\simeq P_i \times \frac{15ml + 30cm \times \pi \times (0.8mm)^2 + 15\mu l}{10ml + 30cm \times \pi \times (0.8mm)^2 + 15\mu l} \\
P_f &\simeq 10^5 \times \frac{15ml + 0.6ml + 15\mu l}{10ml + 0.6ml + 15\mu l} \\
P_f &\simeq 1.47 \times 10^5 Pa
\end{aligned}$$

With these experimental setup and parameters, we could impose a pressure of around 1.5 atmosphere on the solution contained in one reservoir.

We didn't monitor the pressure inside the system, but we could observe that the blow generated we the silicon tubing is unplugged for the syringe is almost as strong after 30 minutes of experiments, as it is after a few seconds. Which we view as an indication of a leaking rate low enough to allow us to consider the pressure to be constant over the course of approximately 6minute-long experiments.

6.3 Pre-concentration of GFP

6.3.1 Experimental setup

We use a solution of GFP at a concentration of 33μM in phosphate buffer with concentration 1mM. The electrical potentials applied are described in figure 6-2. The total pressure applied is indicated above the reservoirs when it is different from the

atmospheric pressure.

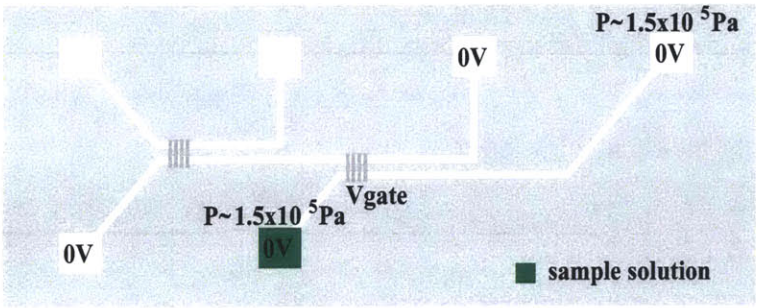

Figure 6-2: Experimental conditions leading to the formation of a pressure plug.

6.3.2 Results

The conditions described above are maintained for a certain amount of time, during which, at regular intervals we take intensity measurements to follow the increase in concentration in GFP plug. A picture of a typical pressure plug is featured below (picture 6-3).

The picture in figure 6-4 shows a fluorescence measurement after 30min applying the experimental conditions described above with a 10mM phosphate buffer. At this buffer concentration, no protein pre-concentration can take place. Consequently, the sample solution was flowing freely through the nanochannels without being hampered. The picture in figure 6-4 then helps us understand the flow pattern in the channels. The leftmost channel on the picture, corresponds to the path of smallest fluidic resistance for the pressure-driven flow. As shown in the graph of figure 6-4, it also corresponds to the channel with the highest remaining fluorescence. We attribute this to the fact that it is the channel through which the flow of buffer and sample was the greatest. The second nanochannel from the left, is the path with the second smallest fluidic resistance, and it is also the channel with the second highest level of remaining adsorbed GFP. From these observations, we can deduce information on the flow pattern in the device.

The pictures show the pressure plug building up with time (picture 6-5. This series of experiment used a 0.5mM phosphate buffer and 11μM GFP solution.

The plots in figure 6-6 measure the evolution of the pressure plug with time. The measurements were made from the same single experiment that is representative of the typical formation of the pressure plug.

6.3.3 Interpretation

For the pressure that we can reach using this setup. The concentration factors appear to be smaller than the factors we could reach using an electrokinetic flow.

It is clear from the pictures, that a plug formed with a half atmosphere additional pressure, is less focused than a electrokinetic plug formed in a $350 V \cdot m^{-1}$ electric field. Meaning that the ratio of the plugs maximum intensity to the plug's width is much smaller in the pressure-induced case.

Considering the fluidic resistances of the deep and shallow channels, we expect the flow rate to be most important in the shortest path from the high pressure reservoirs to the low pressure reservoirs. This is confirmed by the picture in figure 6-4 where a buffer concentration of 10mM prevents any plug from forming. So the GFP sample just flows through the nanochannels. The highest fluorescence in the leftmost nanochannel, which corresponds to the shortest path from high to low pressure reservoir, testifies of a higher GFP flow rate through this channel than through the others. We can see that the hierarchy of flow rates is the one we are expected. The shortest path has the highest flow rate, the second shortest path has the second highest flow rate, etc.

Plots 6-6 show the formation rate of pressure plug. In the case of electrokinetic flow, we observed the charged sample keeping piling up on the existing plug. Whereas in the case of a pressure-induced plug, we can see the plug concentration rate decreasing once a rather low concentration factor is reached. Repeated experiments showed

that this saturation phenomenon was not due to an undesired drop in the applied pressure. Figures 6-6 show that the concentration rate is high in the first few minutes and then after becomes almost zero. The two plots in figure 6-6 are different in the sense that the top plot shows the maximum concentration factor in the plug. Whereas the bottom plot shows the total accumulated amount of GFP in the plug region. The relationship between maximum concentration and total accumulation would have to be sorted out by a simulation of the sample ions concentration distribution in and around the plug.

6.4 Influence of buffer ionic strength on pre-concentration rate

6.4.1 Experimental conditions

The experimental conditions are identical to the ones described in figure 6-2.

6.4.2 Results

As the ionic strength it increased, the concentration factor decreases (figure 6-7).

6.4.3 Interpretation

This experiment is an additional clue to corroborate our interpretation of the pre-concentration phenomenon. A decreasing pre-concentration efficiency as the buffer concentration is increased, is compatible with the theory that Debye layer and depletion region play a major role. The Debye layer thickness is sensitive to the buffer concentration as shown before (2.1.1). It decreases when the ionic strength is increased. Thus the ions selection is weaker and the depletion region that forms is less selective and the pre-concentration of negatively charged GFP becomes less efficient.

6.5 Influence of pressure on pre-concentration rate

6.5.1 Experimental conditions

The experimental conditions are identical to the ones described above (6-2).

6.5.2 Results

We applied additional pressures ranging from 0.07atm to 0.5atm. The setup used to apply pressure is described above in paragraph 6.2.2. No correlation was found between the applied pressure and the concentration rate (figure 6-8).

6.5.3 Interpretation

Let's consider the sample is loaded in reservoir 5, and an additional pressure of 0.5atm is applied to reservoirs R3 and R5. Using the notations of figure 6-9, we would have (V1,V2,V3,V5)=(0,0,5×10^4,5×10^4). We can also calculate the resistance R_0, R_1, R_2, R_3 and R_5. The fluidic resistance of a channel with rectangular cross-section is

$$R = \frac{12\mu L}{wh^3}$$

with μ the viscosity of the fluid in the channel, L the length of the channel, w its width and h its depth ([47]). So we obtain R_0=$5\times10^{20}\Omega$, R_1=$3.5\times10^{19}\Omega$, R_2=$7\times10^{19}\Omega$, R_3=$10.5\times10^{19}\Omega$ and R_5=$3.5\times10^{19}\Omega$.Finally, let's call j_1, j_2, j_3 and j_5 the currents in the resistances R_1, R_2, R_3 and R_5. The positive direction chosen for each current is given in figure 6-9. Then using basic electrical equations we find linear system of equations:

$$\begin{pmatrix} 0 \\ 0 \\ V5 \\ V3 \\ -V1 \\ -V2 \\ 0 \end{pmatrix} = \begin{pmatrix} 0 & 0 & -1 & 1 & 1 & 0 & 0 \\ 1 & 1 & -1 & 0 & 0 & 0 & 0 \\ 0 & 0 & 0 & 0 & R_3 & 0 & 1 \\ 0 & 0 & 0 & R_4 & 0 & 0 & 1 \\ R_1 & 0 & 0 & 0 & 0 & -1 & 0 \\ 0 & R_2 & 0 & 0 & 0 & -1 & 0 \\ 0 & 0 & R_0 & 0 & 0 & 1 & -1 \end{pmatrix} \cdot \begin{pmatrix} j_1 \\ j_2 \\ i \\ j_3 \\ j_5 \\ W1 \\ W2 \end{pmatrix}$$

Solving this system of 7 unknowns and 7 equations, we obtain the pressure difference between the two ends of the nanochannel (W2-W1) as well as the flow rate Q_{nano} through the nanochannels.

$$\begin{pmatrix} j_1 \\ j_2 \\ i \\ j_3 \\ j_5 \\ W1 \\ W2 \end{pmatrix} = \begin{pmatrix} 6.06 \times 10^{-17} m^3.s^{-1} \\ 3.03 \times 10^{-17} m^3.s^{-1} \\ 9.09 \times 10^{-17} m^3.s^{-1}5 \\ 6.82 \times 10^{-17} m^3.s^{-1} \\ 2.27 \times 10^{-17} m^3.s^{-1} \\ 2122.82Pa \\ 47611.83Pa \end{pmatrix}$$

Once this pressure difference between the two ends of the nanochannel is known, we can calculate the streaming current present in the initial moments of the pressure-driven concentration experiments. We know that the coupling between pressure difference and potential difference through a membrane is:

$$\begin{bmatrix} Q_p \\ i_p \end{bmatrix} = \begin{bmatrix} -\frac{\pi h_{ch}^4}{8\eta l_{ch}} & \frac{S_{ch}\epsilon\zeta}{\eta l_{ch}} \\ \frac{S_{ch}\epsilon\zeta}{\eta l_{ch}} & -(\frac{S_{ch}\sigma}{l_{ch}} + \frac{(w_{ch}+h_{ch})\epsilon^2\zeta^2}{\eta h_{ch} l_{ch}}) \end{bmatrix} \cdot \begin{bmatrix} \Delta P \\ \Delta V \end{bmatrix}$$

In our experiment, we impose a potential of 0 to the fluid in reservoirs R1, R2,

R3 and R5, so we have ΔV=0V in the system above and finally:

$$\begin{aligned} i_p &= \frac{S_{ch}\epsilon\zeta}{\eta l_{ch}}\Delta P \\ i_p &= \frac{10\mu m \cdot 62nm \cdot 80 \cdot 8.82 \times 10^{-14} \cdot 100mV}{0.01cPl \cdot 10\mu m \cdot 4.5} \cdot 10^4 \\ i_p &= 1.98 \times 10^{-13} A \simeq 0.2pA \end{aligned}$$

Let's compare this current to the one created by the concentrator operated under electrokinetic flow. The electrical system is identical to the one presented in figure 6-9 with V1=V2=0V, V5=10V and V3=5V. Following the example calculation given in paragraph 2.1.4, we find R_1=R_5=3.3×$10^{10}\Omega$, R_2=6.6×$10^{10}\Omega$ and R_3=9.9×$10^{10}\Omega$. The linear invertible system of equations of dimension 7 is the same as the previous one, and we obtain:

$$\begin{pmatrix} j_1 \\ j_2 \\ i \\ j_3 \\ j_5 \\ W1 \\ W2 \end{pmatrix} = \begin{pmatrix} 1.2 \times 10^{-10} A \\ 6.1 \times 10^{-11} A \\ 1.8 \times 10^{-10} A \\ 8.1 \times 10^{-12} A \\ 1.7 \times 10^{-10} A \\ 4V \\ 4.2V \end{pmatrix}$$

So the current intensity through the nanochannels in the case of an electrokinetic flow is:

$$i_{ek} = 0.2nA.$$

The pressure-induced current through the nanochannels is three orders of magnitude smaller than it is in the case of an electrokinetic flow. This can explain why the ion depletion region is wide enough to be clearly seen in the electrokinetic case and not in the pressure case.

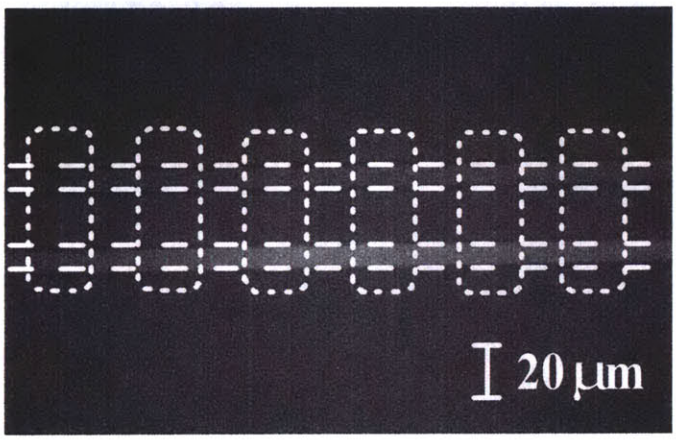

Figure 6-3: Picture of a typical pressure-induced GFP plug in the channel of a silicon device.

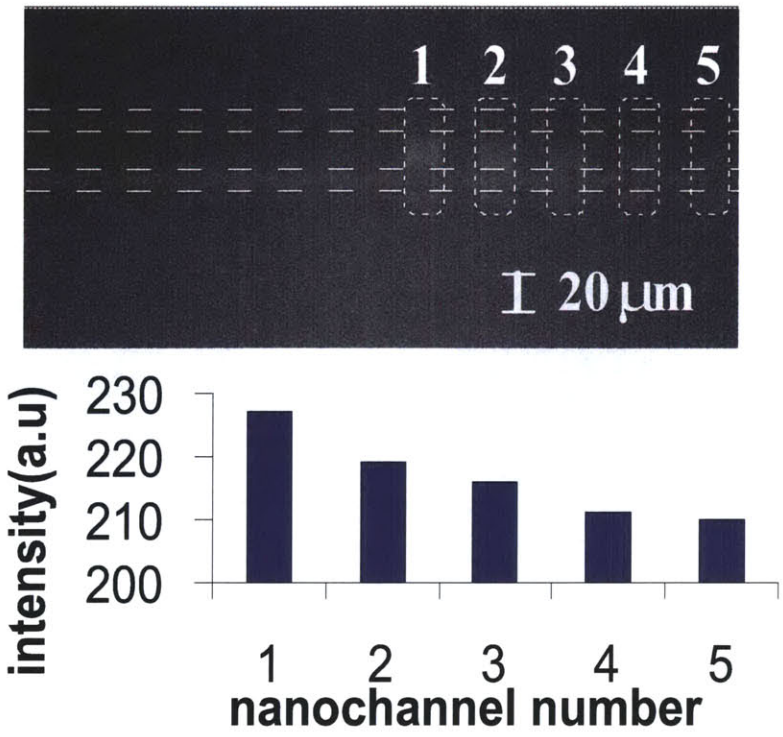

Figure 6-4: Fluorescence measurement for a 11μM GFP sample in 10mM phosphate buffer. The intensity of the adsorbed GFP is greater in the channels corresponding to the smallest fluidic resistance.

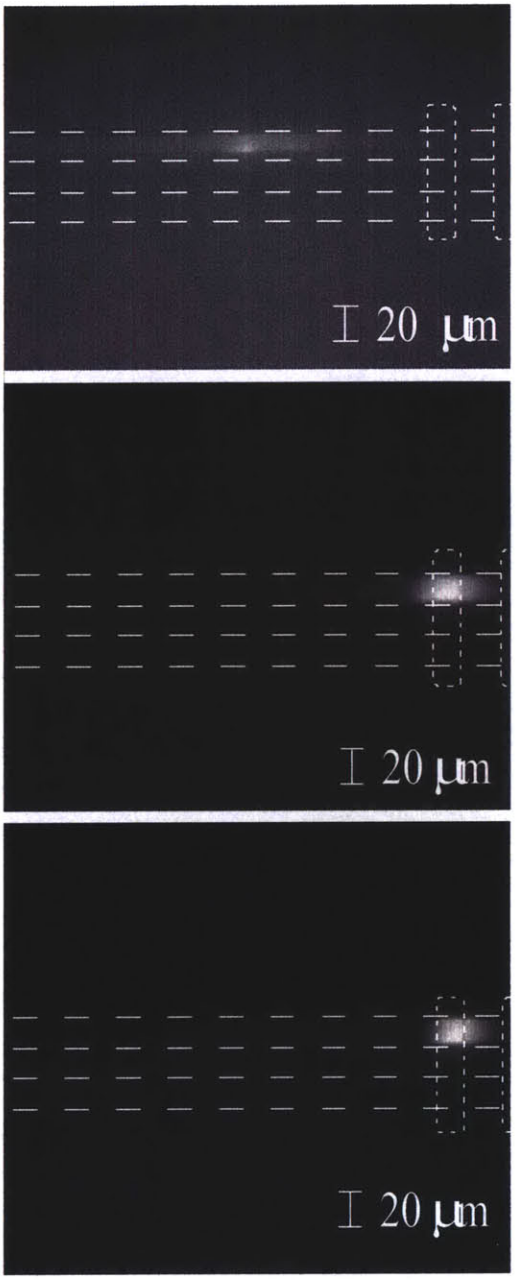

Figure 6-5: Plugs formed after 30 seconds, 3minutes and 6minutes are shown respectively in the top, middle and bottom pictures.

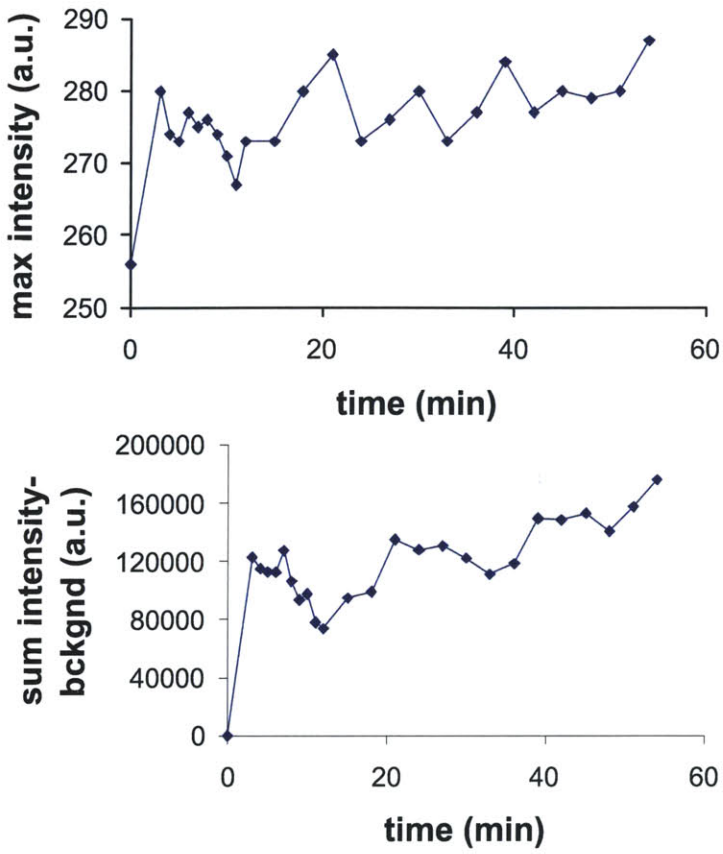

Figure 6-6: Top plot: evolution of the maximum intensity of the pressure plug with time. Bottom plot: evolution with time of the total intensity of the frames when the background intensity is subtracted.

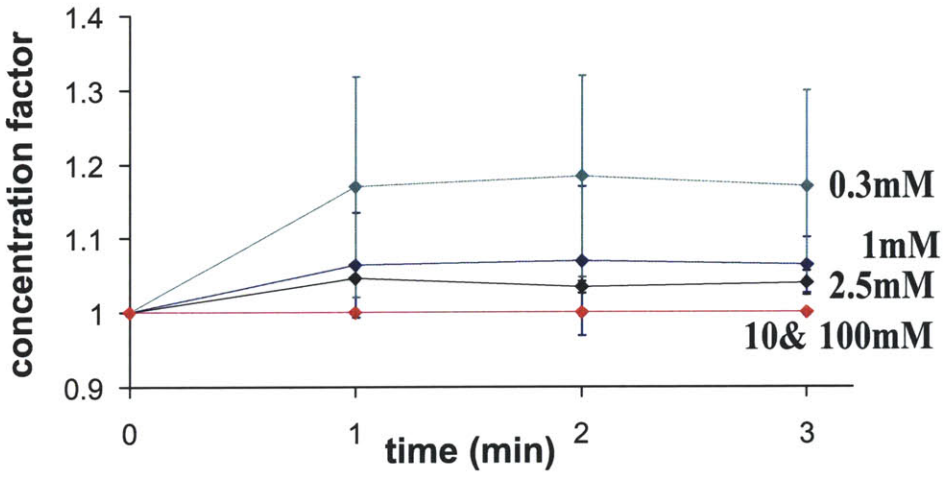

Figure 6-7: Effect of phosphate buffer concentration on the pre-concentration rate. Red line: C_{buffer}=100mM and 10mM; black line: c_{buffer}=2.5mM; blue line: c_{buffer} = $1mM$ and green line: c_{buffer}=0.3mM.

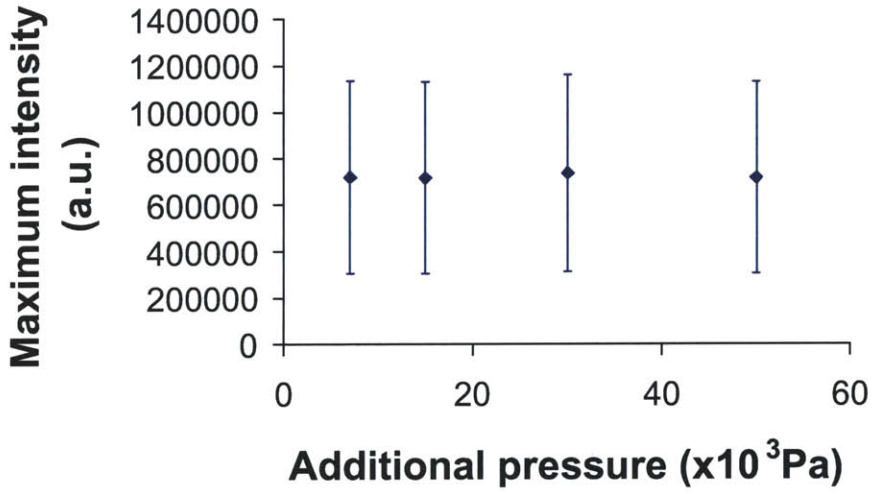

Figure 6-8: Effect of the imposed pressure on the concentration factor.

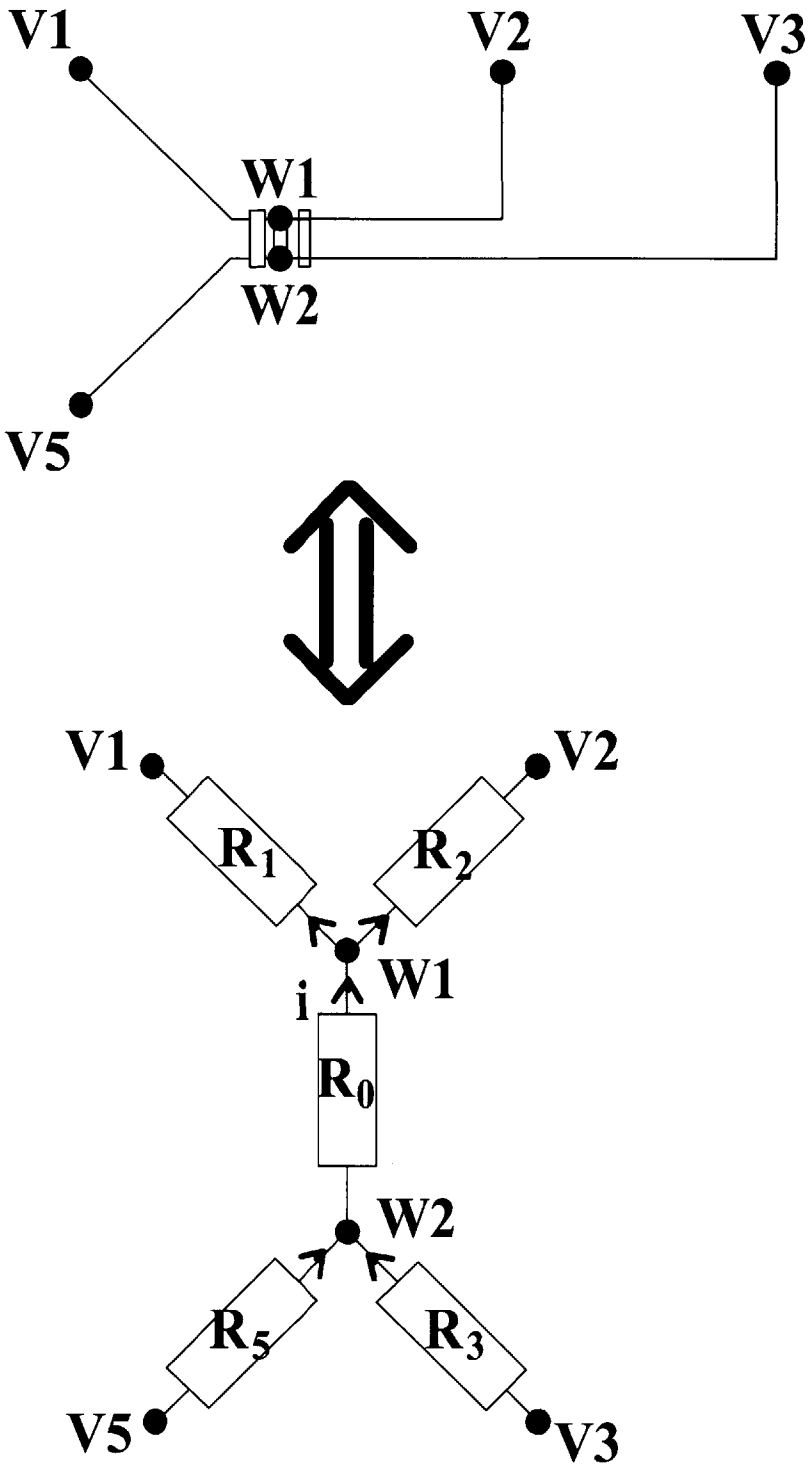

Figure 6-9: Representation of the actual device and its electrical circuit analogy.

Chapter 7

External gate potential control of concentration polarization

The phenomena shown in the previous chapter clearly demonstrate the fluid-field coupling in the nanofluidic channel. In this chapter, we will control this phenomenon by changing the gate potential of the device as in Chapter 5.

7.1 Modification of the depletion region width with the V_{gate}

7.1.1 Experimental conditions

A zero potential is imposed on the solution in all 4 reservoirs used for the experiment. A total pressure of $10^5 + 3 \times 10^4 Pa$ is imposed on two reservoirs in order to drive the flow through the nanochannels (figure 7-1). Once the plug has formed, V_{gate} is changed between -30V and 30V and simultaneously the position of the plug is observed.

7.1.2 Results

The motion of the plug is analogous to the one observed above in paragraph 5.1.2. Increasing V_{gate} moves the plug closer to the nanochannels. Decreasing V_{gate} pushes

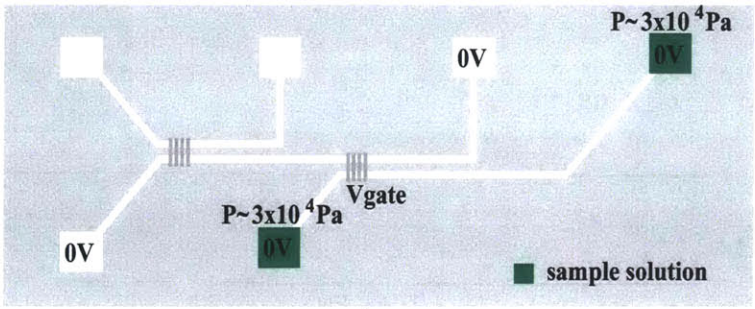

Figure 7-1: Electrical potentials and additional pressure used for the experiment.

the plug away from the nanochannels.

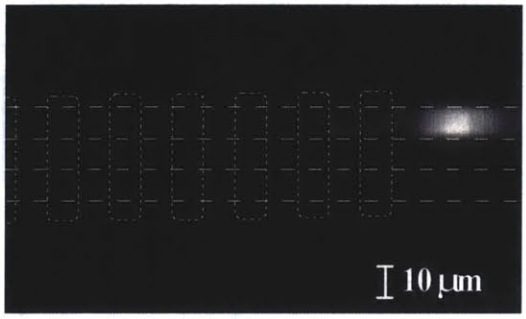

Figure 7-2: Pressure plug obtained after 4minutes in the experimental conditions described in paragraph 7.1.1.

7.1.3 Interpretation

As we expected, the change in driving mechanism doesn't alter the interpretation made in paragraph 5.1.3. In a similar fashion, a decreased V_{gate} creates a more negative surface charge, which in turn creates a larger double layer. This makes the ionic current imbalance through the shallow channels more stringent. A stronger charge polarization creates in turn a large depletion region. The sample consists of co-ions that are trapped at the boundary of this depletion region and consequently pushed further away from the channels as V_{gate} is decreased.

The exact opposite argument can be made to account for the plug getting closer to

the gates as $Vgate$ is increased.

7.2 Influence of V_{gate} on the pre-concentration rate

7.2.1 Experimental conditions

The experimental conditions are identical to the ones described above (7.1.1).

We let the system run under these experimental conditions for various values of V_{gate}. After 3 minutes, a picture is taken to measure the concentration of the plug that we created.

7.2.2 Results

We could observe a an increase in the concentration of the plug created as V_{gate} was decreased beneath a threshold (here $\sim$15V).

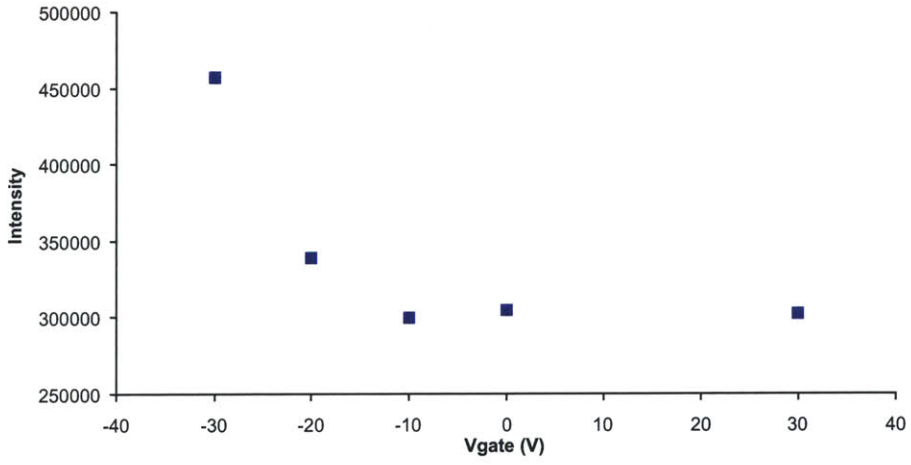

Figure 7-3: Intensity of the plug obtained after 3 minutes of pre-concentration for several values of V_{gate}. The flow is pressure-driven.

The series of pictures 7-4 shows plugs formed for different values of V_{gate}.

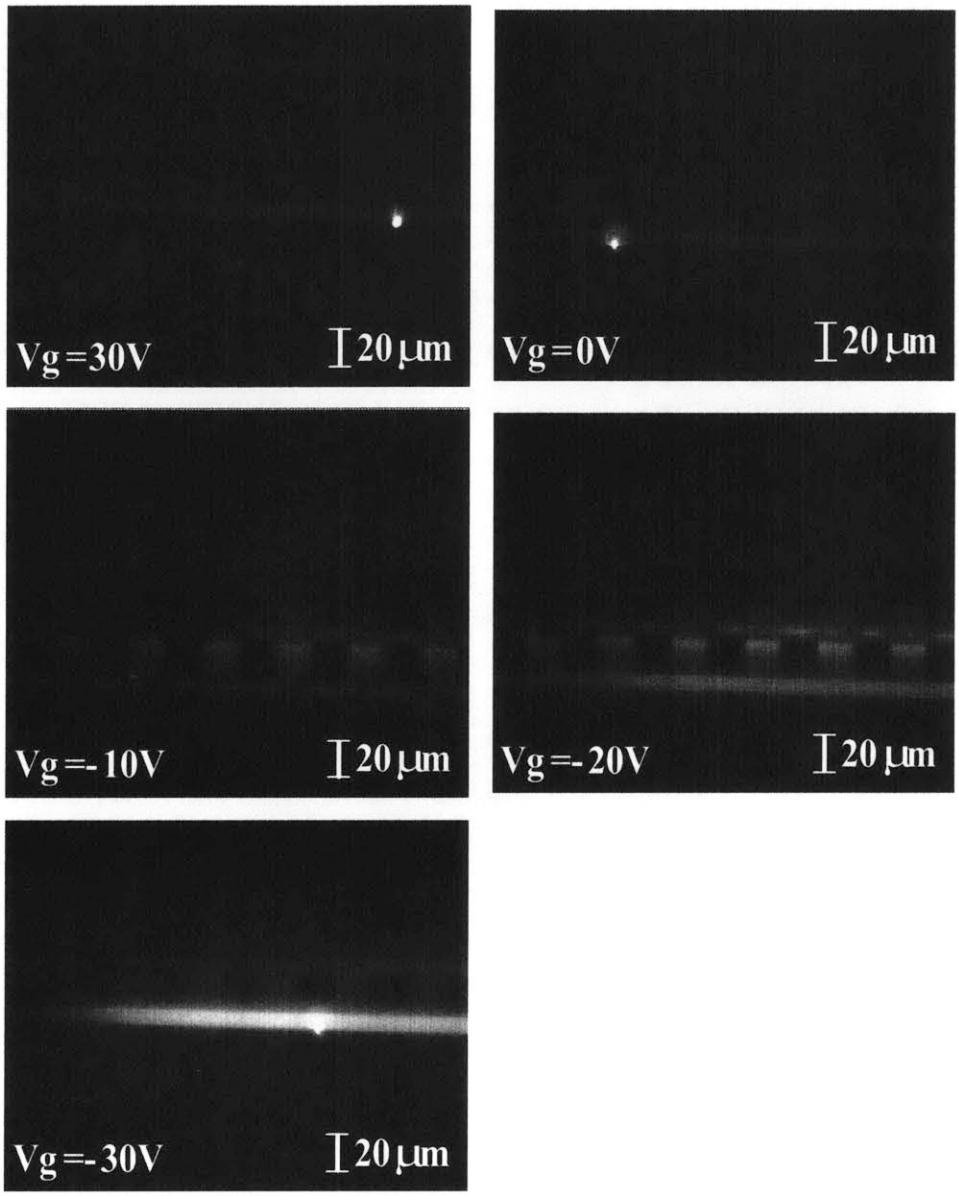

Figure 7-4: Plug formed under the conditions described in paragraph 7.1.1 after 3 minutes and with V_{gate} set to 30V, 0V, -10V, -20V and -30V.

7.2.3 Interpretation

As described in the previous interpretation sections, we can interpret this trend by noting that the lower the gate voltage, the wider the double layer in the nanochannels. And then the wider the double layer, the more efficient the charge selectivity ([35]). This difference in transport numbers of co-ions and counter-ions creates charge polarization zones. One depleted and one concentrated respectively at the cathodic and anodic sides of the nanochannels. So when V_{gate} is decreased, the nanochannel becomes more permselective and the plug forms faster.

It is interesting to confirm that the same concentration/fitlering phenomenon is taking place as in the case of an electrokinetic flow, apparently independently of the mechanism driving the flow.

Chapter 8

Conclusion

We re-demonstrated preconcentration capabilities of nanochannels with overlapping double layers in the case of electrokinetic flows, and demonstrated it in the case of a pressure-driven flow. These initial experiments were followed by an investigation of the effect of the gate potential of the concentration rate for both driving mechanisms. We could indeed measure the impact of the gate potential on the concentrator.

We attributed these experimental observations to different transport numbers for co-ions and counter-ions through nanochannels (permselectivity). Which create a depleted charge polarization region at the boundary of which co-ions can be concentrated if they are driven towards this region by electrokinetic flows or pressure.
We interpreted the effect of the external gate potential control on the concentration using simple models that link the surface charge density to the applied gate potential. Decreasing the applied voltage, increases the negative surface charge on the channel walls and the double layer thickness. Which in turns makes the nanochannels more permselective and facilitates a faster preconcentration. This interpretation was corroborated by experimental measures of the position of the concentration plugs with respect to the nanochannels, and by varying the ionic strength of the buffer.

Some challenges remain though. The most important is to decrease adsorption of sample on the channel walls and thus extend the lifespan of each device. Shortage of

material means prevented the realization of coating experiments.

Nanochannels concentrating possibilities were re-demonstrated in the case of electrokinetic flow and demonstrated in the case of pressure-driven flow. Moreover the efficiency of their control by an externally applied gate potential was measured and opens the way for feedback loops and other real time tunings of the concentrator's performance.

Appendix A

PDMS device fabrication

A.1 Photolithography masks

The mask was drawn using the CAD software L-Edit (Tanner EDA, Pasadena, CA) and printed on a transparency foil by OutPutCity (Poway, CA).

A.2 Photolithography to fabricate silicon masters

At this stage we want to have to mask fabricated using the technique described above. One mask features the thin channels and the other the deep channels. The silicon processing step will now aim at transfering these two patterns into bulk silicon. We start off by cleaning the masks and a 6 inch silicon wafer with ethanol and DI water. The photolithography process we are using is called image reversal. We spin coat the silicon wafer with Clariant AZ 5214 positive photoresist at 7000rpm for 30s.

Figure A-1: Spun photoresist (AZ 5214).

The wafer is soft baked for 30 minutes at 90°C before being exposed to UV light, through the shallow channel mask, for 2 seconds with intensity 10mW/cm2/s. The

photoresist is the post-baked for 20 minutes at 95°C before being flood exposed to UV light for 45s, without mask, and with the same intensity as above.

Figure A-2: Exposed photoresist.

We can now developp the photoresist using the Clariant developper AZ 422 for about 1min.

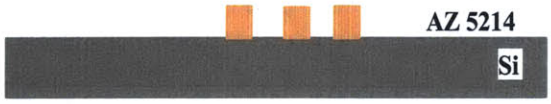

Figure A-3: Developed photoresist.

Under the microscope, we check the resolution of the features we patterned into photoresist. We now want to etch them into silicon. We are using SF6 and oxygen to etch silicon. The photoresist ectch rate is two thirds of that of silicon: 200nm/min compared to 330 nm/min.

Figure A-4: Etched photoresist and silicon.

In order to remove the remaining photoresist, we use an asher that attacks the chemical by exposing it to the reactivity and kinetic energy of oxygen ions in an oxygen plasma generated by a 1200W 13.5MHz power supply. It is sometimes necessary to pyranha the wafer in a wet station to remove the remaining photoresist.

At this point we have the thin channel patterns engraved in the silicon wafer. We can now concentrate on the deep channels. We will use a photoresist that can be

Figure A-5: Etched silicon.

spun in thicker layers (10um at 3000rpm): the MicroChem SU-8 10.

*** receipe in lab book*** 11 - Soft bake 12 - Initial exposure through the deep channel mask 13 - Post-exposure bake: 15 - Developpement of the unexposed photoresist *** receipe in lab book***

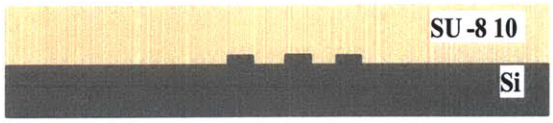

Figure A-6: Spun photoresist (SU-8 10).

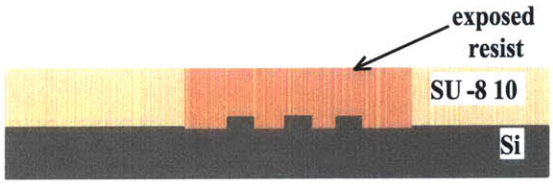

Figure A-7: Exposed photoresist.

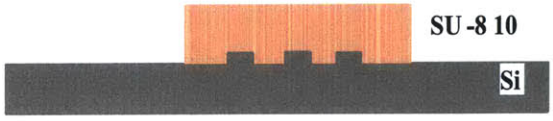

Figure A-8: Developed photoresist.

Figure A-9: Etched photoresist and silicon.

Figure A-10: Cleaned silicon wafer featuring shallow and deep channels.

Then we can either use the wafer with SU-8 photoresist left on top as a master or etch the photoresist in order to have both thin and deep channels engraved into silicon. Hard bake in a convection oven further cross-links the material so it can be part of the final device.

A.3 Electrodes fabrication

We use photolithography on thin pyrex wafers to fabricate the gold electrodes. We start the process with the image-reversal technique described above (A.2).

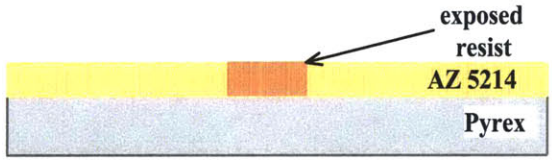

Figure A-11: Image reversal process using AZ 5214 on a pyrex wafer.

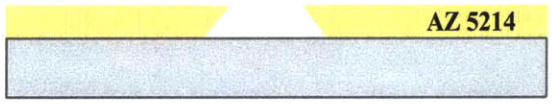

Figure A-12: Developed photoresist.

The adhesion of gold to pyrex is very weak, so we have to use a titanium layer as an adhesion promoter. The ratio we used is 15nm Ti for 120nm Au. eBeam deposition covers the whole wafer with first a titanium layer and second a gold layer.

Then we use a lift-off process to get rid of the photoresist covered with Ti-Au layers. Acetone is the solvent we used. Thus only the electrodes with the desired

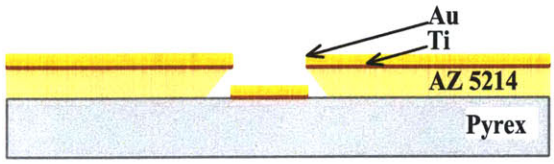

Figure A-13: eBeam deposition of a titanium and a gold layer.

pattern are left on the wafer.

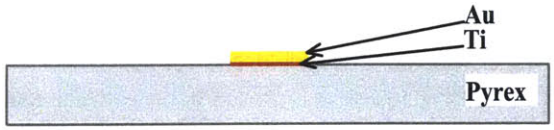

Figure A-14: Lift-off process leaves only the patterned gold electrodes on the pyrex wafer.

Finally cover the electrodes with a layer of dielectric material: SiO_2. This layer is aimed at reducing the bubble generation in the channel.

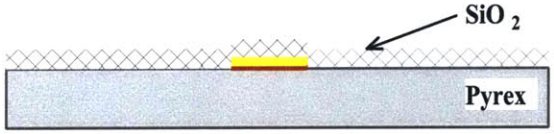

Figure A-15: Final electrode cross-section.

A.4 PDMS Fabrication

The silicon wafers we micro-fabricated are used as masters on which the poly(dimethylsiloxane) polymer is molded. We can use two recipes. One is a simple mix in a 10:1 mass ratio of PDMS and Sylgard 184. And the other that provides a more rigid polymer (hard-PDMS) ([48]), uses a modulator and a catalyst in addition to a vinyl compound and a hydrosilane component. Once we have opted for h-PDMS, we still have the choice between using only h-PDMS, which makes rather brittle devices. Or Spinning a thin

layer of h-PDMS on which we later pour a thicker layer of conventional PDMS. This polymer is degassed in a vacuum chamber before being poured over the wafers and baked for 24 hours at 65°C. The peel-off step is made easier if the wafer was coated with silane (a few drops of silane adhesion promoter under vacuum for 2h.)

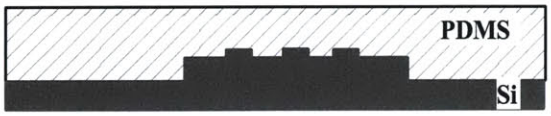

Figure A-16: Molding of PDMS on the silicon wafer.

A.5 PDMS to glass bounding

Figure A-17: Cross section of the PDMS device.

Appendix B

Silicon device fabrication process flow

General process: nanochannels with various depths are patterned and etched into silicon wafers by photolithography and reactive ion etching techniques. Potassium hydroxide (KOH) etching is used to make access hole through the wafer. A thermal oxide is grown to provide an electrical isolation between silicon substrate and buffer solution. Finally, the silicon wafer is bonded to a Pyrex wafer using anodic bonding technique.

Starting material: clean 6" ¡100¿ silicon wafer (single side polished)

Refer to table for detailed process steps.

Step	Fab	Machine	Action
1	ICL	Coater6	Spin coating wafer with Shipley SPR-1.0
2	TRL	EV1	Expose resist (alignment mark mask)
3	ICL	Coater6	Develop the resist
4	ICL	AME5000	RIE etch silicon for alignment mark (1μm)
5	ICL	Asher	Strip remaining photoresist
6	ICL	Pre-metal	Piranha cleaning
7	ICL	P-10	Depth measurement
8	ICL	RCA	Standard RCA cleaning
9	ICL	VTR	Low-stress silicon nitride deposition (1000 Å)
10	ICL	Coater6	Spin coating afer with Shipley SPR-1.0
11	ICL	EV1	Expose resist (access hole mask)
12	ICL	Coater6	Develop the resist
13	ICL	AME5000	RIE etch SiN to open loading holes
14	ICL	Asher	Strip photoresist
15	ICL	TMAH-KOH hood	KOH etching silicon access holes
16	ICL	Pre-metal	Post-KOH cleaning
17	ICL	NitrEtch-HotPros	Silicon Nitride Removal
18	ICL	RCA	Standard RCA pre-furnace cleaning
19	ICL	5C-FieldOx	Thermal oxidation (400nm)
20	ICL	Acidhood	Silicon and Pyrex wafer cleaning
21	ICL	EV501	Anodic bounding
22	ICL	Diesaw	Diesaw cutting

Table B.1: Detailed process steps.

Bibliography

[1] H.J. Craighead J. Han. Separation of long dna molecules in a microfabricated entropic trap array. *SCIENCE*, 286:1026–1029, 1998.

[2] C.R. Martin M. Nishizawa, V.P. Menon. Metal nanotubule membranes with electrochemically switchable ion-transport selectivity. *SCIENCE*, 268:700–702, 1995.

[3] S. Y. Lee S. J. Lee. Micro total analysis system (μ-tas) in biotechnology. *Applied Microbiology Biotechnology*, pages 289–299, 2004.

[4] D. Branton D.W. Deamer J.J. Kasianowicz, E. Brandin. Characterization of individual polynucleotide molecules using a membrane channel. *Proceedings of the National Academy of Science of the United States of America*, 93:13770–13773, 1996.

[5] L. L. Sohn O. A. Saleh. Quantitative sensing of nanoscale colloids using a microchip coulter counter. *Review of Scientific Instruments*, 72:4449–4451, 2001.

[6] A. Lopez H. G. Craighead S. W. Turner, A. M. Perez. Monolithic nanofluid sieving structures for dna manipulation. *Journal of Vacuum Science and Technology B*, 16:3835–3840, 1998.

[7] P.-A. Auroux A. Manz D.R. Reyes, D. Iossifidis. Micro total analysis systems. 1. introduction, theory, and technology. *Analytical Chemistry*, 74:2623–2636, 2002.

[8] D.R. Reyes A. Manz P.-A. Auroux, D. Iossifidis. Micro total analysis systems. 2. analytical standard operations and applications. *Analytical Chemistry*, 74:2637–2652, 2002.

[9] Andreas Manz Torsten Vilkner, Dirk Janasek. Micro total analysis systems. recent developments. *Analytical Chemistry*, 76:3373–3386, 2004.

[10] J. Han J. Fu, P. Mao. Gel-free size separation of biomolecules by regular nanofluidic molecular filter array. *to be submitted.*

[11] D.W. Austin T. Sims M. A. Guillorn M.L. Simpson T.E. McKnight, A.V. Melechko. Microarrays of vertically-aligned carbon nanofiber electrodes in an open fluidic channel. *Journal of Physical Chemistry*, 22:7115–7125, 2004.

[12] T. Kramer J.W. Berenschot A. Van Den Berg N.R. Tas, P. Mela. Capillarity induced negative pressure of water plugs in nanochannels. *Nano Letters*, 3(11):1537–1540, 2003.

[13] Ronald F. Probstein. *Physicochemical Hydrodynamics. An Introduction. Second Edition.* Wiley Interscience, 2003.

[14] S.C. Jacobson N.J. Petersen J.M. Ramsey, J.P. Alarie. In Kluwer Academic Publishers, editor, *Micro Total Analysis Systems, Nara, Japan*, pages 314–316, 2002.

[15] S.C. Jacobson J.M. Ramsey N.J. Petersen, J.P. Alarie. In Kluwer Academic Publishers, editor, *Micro Total Analysis Systems, Squaw Valley, CA, USA*, pages 314–316, 2003.

[16] J. Hendrikse A. van den Berg R.B.M. Schasfoort, S. Schlautmann. Field-effet flow control for microfabricated fluidic networks. *SCIENCE*, 286:942–945, 1999.

[17] C.-T. Wu C.S. Lee, W.C. Blanchard. Direct control of electroosmosis in capillary zone electrophoresis by using an external electric field. *Analytical Chemistry*, 62:1550–1552, 1990.

[18] M.A. Hayes N.A. Polson. Electroosmotic flow control of fluids on a capillary electrophoresis microdevice using an applied external voltage. *Analytical Chemistry*, 72:1088–1092, 2000.

[19] R.S. Underhill C.A. Lucy. Characterization of the cationic surfactant induced reversal of electroosmotic flow in capillary electrophoresis. *Analytical Chemistry*, 68:300–305, 1996.

[20] C.-T. Wu B. Patel C.S. Lee, D. McManigill. Factors affecting direct control of electroosmosis using an external electric field in capillary electrophoresis. *Analytical Chemistry*, 63:1519–1523, 1991.

[21] J. Han Y.-C. Wang. Million-fold concentration of proteins and peptides by nanofluidic filter. *to be published.*

[22] R.J. Hunter. *Zeta Potential in Colloid Science.* Academic Press, 1981.

[23] A. J. Grodzinsky. *Fields, Forces and Flows in Biological Systems.* Massachusetts Institute of Technology, 2003.

[24] H. Morgan N. G. Green. Dielectric investigations of submicrometre latex spheres. *Journal of Physics D: Applied Physics*, 30:2626–2633, 1997.

[25] A.G. Ewing M.A. Hayes. Electroosmotic flow control and monitoring with an applied radial voltage for capillary zone electrophoresis. *Analytical Chemistry*, 64:512–516, 1992.

[26] A.G. Ewing M.A. Hayes, I. Kheterpal. Electroosmotic flow control and surface conductance in capillary zone electrophoresis. *Analytical Chemistry*, 65:2010–2013, 1993.

[27] D.L. DeVoe C.S. Lee J.S. Buch, P.-C. Wang. Field-effect flow control in a polydimethylsiloxane-based microfluidic system. *Electrophoresis*, 22:3902–3907, 2001.

[28] A.G. Ewing M.A. Hayes, I. Kheterpal. Effects of buffer ph on electroosmotic flow control by an applied radial voltage for capillary zone electrophoresis. *Analytical Chemistry*, 65:27–31, 1993.

[29] W.T. Kok H. Poppe, A. Cifuentes. Theoretical description of the influence of external radial fields on the electroosmotic flow in capillary electrophoresis. *Analytical Chemistry*, 68:888–893, 1996.

[30] M.A. Hayes N.K. Hartley. Examination of theoretical models in external voltage control of capillary electrophoresis. *Analytical Chemistry*, 74:1249–1255, 2002.

[31] B. Van den Bossche L. Bortels A. Van Theemsche, J. Deconinck. Numerical solution of a multi-ion one potential model for electroosmotic flow in two-dimensional rectangular microchannels. *Analytical Chemistry*, 74:4919–4926, 2002.

[32] S. Schlautmann Ph. Renaud A. van den Berg Y.-S. Leung Ki, R.B.M. Schasfoort. Modeling of flowfet characteristics. In Nano Science and Technology Institute, editors, *Technical Proceedings of the 2000 International Conference on Modeling and Simulation of Microsystems*, 2000.

[33] L. Bortels A.V. Theemsche, J. Deconinck. Numerical simulation of electroosmotic flow in a 'flow field effect transistor'. *Electrochimica Acta*, 48:3307–3312, 2003.

[34] H.H. Hu N.A. Pantakar. Numerical simulation of electroosmotic flow. *Analytical Chemistry*, 70:1870–1881, 1998.

[35] A. Majumdar H. Daiguji, P. Yang. Ion transport in nanofluidic channels. *Nano Letters*, 4(1):137–142, 2004.

[36] I. Nischang U. Tallarek, F.C. Leinweber. Perspective on concentration polarization effects in electrochromatographic separations. *Electrophoresis*, 26:391–404, 2005.

[37] P. Mao. Fabrication and characterization of nanofluidic channels for studying molecular dynamics in confined environments. Master's thesis, M.I.T., February 2005.

[38] BD Biosciences Clontech. Living colors, user manual.

[39] H. G. Craighead J. Han. Entropic trapping and sieving of long dna molecules in a nanofluidic channel. *Journal of Vacuum Science and Technology A*, 17:2142–2147, 1999.

[40] J. Han P. Mao. Fabrication and characterization of 20 nm nanofluidic channels by glass-glass and glass-silicon bonding. to be submitted.

[41] M.E. Green Y. Fang, Q.L. Li. Hydrodynamic flow and turbulence at the electrodialysis membrane-solution. *ANNALS OF THE NEW YORK ACADEMY OF SCIENCES*, 404:170–173, 1983.

[42] I. Rubinstein. Solutions of nernst-planck-poisson equations in the context of concentration polarization at the cation-exchange membranes. *ANNALS OF THE NEW YORK ACADEMY OF SCIENCES*, 404:475–476, 1983.

[43] B. Zaltzman I. Rubinstein. Electro-osmotic slip of the second kind and instability in concentration polarization at electrodialysis membranes. *Mathematical Models and Methods in Applied Sciences*, 11:263–300, 2001.

[44] P. Taylor. *Advances in Colloid and Interface Science*, volume 35. Elsevier Science Publishers B.V., 1991.

[45] S.S. Dukhin N.A. Mishchuk. *Electrokinetic phenomena of the second kind.*

[46] P.V. Takhistov N.A. Mishchuk. Electroosmosis of the second kind. *Colloids and Surfaces A: Physicochemical and Engineering Aspects.*

[47] G.T.A. Kovacs. *Micromachined Transducers Sourcebook.* WCB McGraw-Hill, 1998.

[48] B. Michel H. Scmidt. Siloxane polymers for high-resolution, high-accuracy soft lithography. *Macromolecules*, pages 3042–3049, 2000.

3526.54